

Learning-based augmentation of first-principle models: A linear fractional representation-based approach [★]

Jan H. Hoekstra ^a, Bendegúz M. Györök ^b, Roland Tóth ^{a,b}, Maarten Schoukens ^a

^a*Control Systems Group, Eindhoven University of Technology, The Netherlands*

^b*Systems and Control Lab, HUN-REN Institute for Computer Science and Control, Budapest, Hungary*

Abstract

Nonlinear system identification has proven to be effective in obtaining accurate models from data for complex real-world systems. In particular, recent encoder-based methods with *artificial neural network state-space* (ANN-SS) models have achieved state-of-the-art performance on various benchmarks, using computationally efficient methods and offering consistent model estimation in the presence of noisy data. However, inclusion of prior knowledge of the system can be further exploited to increase (i) estimation speed, (ii) accuracy, and (iii) interpretability of the resulting models. This paper proposes a model augmentation method that incorporates prior knowledge from *first-principles* (FP) models in a flexible manner. We introduce a novel *linear-fractional-representation* (LFR) model structure that allows for the general representation of various augmentation structures including the ones that are commonly used in the literature, and an encoder-based identification algorithm for estimating the proposed structures together with appropriate initialisation methods. The performance and generalisation capabilities of the proposed method are demonstrated on the identification of a hardening mass-spring-damper system in a simulation study and on the data-driven modelling of the dynamics of an F1Tenth electric car using measured data.

Key words: Nonlinear System Identification; Model Augmentation; Physics-Based Learning.

1 Introduction

As control systems are becoming more complex and performance requirements surge, the need for accurate nonlinear models capable of efficiently capturing complicated behaviours of physical systems is rapidly increasing. It is common practice to derive baseline models using *first-principle* (FP) methods, e.g., rigid body dynamics [30]; however, these models provide only an approximate system description. Although more accurate FP models can be developed, this is a labour-intensive process, especially when additional physical effects—such as friction or aerodynamic forces—are included. Modelling these phenomena from first principles

often requires dedicated experimental campaigns to identify and estimate the associated unknown parameters. Furthermore, the resulting models may become too complex to be handled analytically. In some cases, reliable FP descriptions of the to-be-modelled effects may not even exist, resulting in approximations with varying levels of fidelity.

To overcome these issues, *nonlinear system identification* (NL-SI) methods offer an alternative option to estimate models directly from measurement data [30]. Black-box models, particularly those that incorporate *artificial neural networks* (ANNs), have achieved unprecedented accuracy in capturing complex behaviours. In control applications, ANN-based *state-space* (SS) models have proven to be effective in handling high-order systems and capturing complex nonlinear dynamics [5].

Although black-box methods may result in accurate models, they also have serious downsides. First, flexible function approximators are difficult to interpret, leading to model behaviour that is not well understood. This in turn limits the reliability of the model during, e.g., extrapolation beyond the training data. This is a significant drawback for control applications, where interpretable models are preferred in the design process [10, 25]. The second drawback is the significant time spent learning expected behaviour that has already been modelled thoroughly, e.g., FP-based understanding of the rigid-body-dynamics of the system.

[★] This paper was not presented at any IFAC meeting. Implementation of the proposed method is available at <https://github.com/JanHHoekstra/Model-Augmentation-Public>. This work is funded by the European Union (Horizon Europe, ERC, COMPLETE, 101075836) and has also been supported by the Air Force Office of Scientific Research under award number FA8655-23-1-7061. Views and opinions expressed are however those of the authors only and do not necessarily reflect those of the European Union or the European Research Council Executive Agency. Neither the European Union nor the granting authority can be held responsible for them.

Email addresses: j.h.hoekstra@tue.nl (Jan H. Hoekstra), gyorokbende@sztaki.hun-ren.hu (Bendegúz M. Györök), r.toth@tue.nl (Roland Tóth), m.schoukens@tue.nl (Maarten Schoukens).

Physics-informed neural networks [28] and physics-guided neural networks [11] embed the prior knowledge of the physics in the form of equations (algebraic or partial differential) in the cost function, enforcing the learnt functions to fit to known physics behaviour. This leads to more interpretable models as the known physics are enforced, and shows faster learning convergence. These methods, however, require the knowledge of such physics equations and still rely on a black-box model to capture the entire system.

A promising approach is model augmentation, e.g., [16, 17, 33, 35]. This method combines baseline models with flexible function approximators, such as ANNs, in a combined model structure. As a result of this structural combination, the prior knowledge is directly captured in the baseline model and the learning components only need to model unknown dynamics. For control engineering, such a structure is beneficial, as it is clear how a well-understood baseline model is combined with black-box elements.

In the literature, there are a variety of different model augmentation structures, such as parallel [35] and series [16, 17, 33] interconnections. These interconnections reflect in what form the known baseline model is combined with the learning component that models the unknown behaviour of the system. Although different interconnections may result in an equally accurate model, model complexity and convergence speed also need to be considered, especially when the final model is utilised for control purposes. One interconnection may be equally accurate while having a less complex parameterisation compared to others. It is not trivial to determine which interconnection is the most advantageous for a specific baseline model and data-generating system, as the choice of the optimal interconnection depends on the unknown dynamics of the system. To address this, further research into model augmentation methods is required to develop, e.g., automatic model selection methods. To facilitate this research, a general model augmentation structure is required, such that model augmentation methods can be developed efficiently and compared across different works in literature. Such a general model augmentation structure is currently lacking in the literature.

To solve this problem, a general model augmentation structure based on a *Linear Fractional Representation* (LFR) is proposed, which has been chosen for its modular and flexible nature, enabling a generalised form for augmenting the FP or the already known dynamics. The formulation of LFRs allows for systematic model augmentation while maintaining a clear separation between the baseline and learning components. The proposed model augmentation structure is able to express a wide range of model augmentation structures used in literature, and thus is a unified representation. Furthermore, LFRs are commonly used in the robust control field for uncertainty modelling in a generalised plant format. Thus, in addition to the general representation, the proposed structure also ensures compatibility with well-established control methodologies for classical LFRs [40], making them a versatile choice for a wide range of applications. The price of the uniform model structure is that well-posedness problems

may arise. To address this, we examine the computational graph of the proposed structure and provide well-posedness conditions based on this graph. We also propose an identification algorithm capable of handling the general LFR model augmentation structure with consistency guarantees, while also addressing the joint identification of both the baseline model and learning component parameters and managing overparameterisation through a physics-guided regularisation method.

The main contributions are summarised as¹:

- We present a novel, general LFR-based model augmentation structure with two possible parameterisations: one fully parameterised, offering high flexibility in estimation at the cost of model interpretability, and the other structured and sparsely parameterised, promoting transparency, but requiring more prior knowledge to define the structure;
- We provide proof of the representation capability of the proposed LFR-based model augmentation structure, demonstrating that it is capable of representing all commonly used model augmentation structures in the existing literature;
- We provide conditions under which well-posedness of the proposed model structure is guaranteed;
- We provide an efficient identification algorithm for data-driven estimation of the augmented models under the proposed structure with consistency guarantees.
- We perform rigorous simulation and real-world measurement based studies to validate the proposed methodology.

The paper is organised as follows: first, the system identification problem and available model augmentation approaches are presented in Section 2. Then, Section 3 introduces the LFR-based model augmentation structure and its computational graph. Section 4 provides conditions under which well-posedness of the model is proven. Next, Section 5 provides an identification algorithm with consistency guarantees. A hardening *mass-spring-damper* (MSD) simulation example and real-world experiments with an F1Tenth electric car are used to demonstrate the performance of the proposed identification method in Sections 6 and 7, respectively. The conclusions are given in Section 8.

2 Model Augmentation Problem Setting

We consider the system to be identified given by the *discrete-time* (DT) nonlinear representation

$$x_{k+1} = f(x_k, u_k), \quad (1a)$$

$$y_k = h(x_k, u_k) + e_k, \quad (1b)$$

where $x_k \in \mathbb{R}^{n_x}$ is the state, $u_k \in \mathbb{R}^{n_u}$ is the input, $y_k \in \mathbb{R}^{n_y}$ is

¹ A preliminary version of the methods discussed in this work was presented in [20]. Compared to [20], the key differences are the full parameterisation of the LFR, the computational graph, a detailed well-posedness condition, an extended description of the identification algorithm, a more in-depth simulation study, and a real-world identification example using measured data.

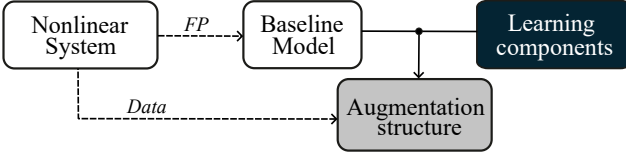


Fig. 1. Learning-based model augmentation concept.

the output signal of the system at time moment $k \in \mathbb{Z}$ with e_k an i.i.d. white noise process with finite variance, representing measurement noise, $f : \mathbb{R}^{n_x} \times \mathbb{R}^{n_u} \rightarrow \mathbb{R}^{n_x}$ is the state-transition function and $h : \mathbb{R}^{n_x} \rightarrow \mathbb{R}^{n_y}$ is the output function. This state-space representation is a general form that can describe a wide range of dynamics encountered in practice.

We assume a baseline model of (1) is available in the form

$$x_{b,k+1} = f_{\text{base}}(\theta_{\text{base}}, x_{b,k}, u_k), \quad (2a)$$

$$\hat{y}_k = h_{\text{base}}(\theta_{\text{base}}, x_{b,k}, u_k), \quad (2b)$$

where $x_{b,k} \in \mathbb{R}^{n_{x_b}}$ is the baseline model state, $\hat{y}_k \in \mathbb{R}^{n_y}$ is the model output, and $f_{\text{base}} : \mathbb{R}^{n_{x_b}} \times \mathbb{R}^{n_u} \rightarrow \mathbb{R}^{n_{x_b}}$ with $h_{\text{base}} : \mathbb{R}^{n_{x_b}} \times \mathbb{R}^{n_u} \rightarrow \mathbb{R}^{n_y}$ are the baseline state-transition and output readout functions respectively, parameterised by $\theta_{\text{base}} \in \mathbb{R}^{n_{\theta_{\text{base}}}}$. The parameters θ_{base} correspond to the physical parameters associated with system (1).

In model augmentation, the baseline model is combined with learning components in a combined model structure. The parameters of this model augmentation structure are then estimated using data measurements of the system as shown in Fig. 1. The general model augmentation structure is described as

$$x_{b,k+1} = (f_{\text{base}} \star f_{\text{aug}})(x_{b,k}, x_{a,k}, u_k), \quad (3a)$$

$$x_{a,k+1} = g_{\text{aug}}(x_{b,k}, x_{a,k}, u_k), \quad (3b)$$

$$\hat{y}_k = (h_{\text{base}} \star h_{\text{aug}})(x_{b,k}, x_{a,k}, u_k), \quad (3c)$$

where $x_{a,k}$ are additional states added for dynamic augmentations, and f_{aug} , g_{aug} and h_{aug} are the learning components parameterised by $\theta_{\text{aug}} \in \mathbb{R}^{n_{\theta_{\text{aug}}}}$. For notational simplicity, both θ_{base} and θ_{aug} are not written out in (3). The operator \star represents an interconnection between two functions. This interconnection can represent a variety of different forms of model augmentation structure used in the literature, such as static parallel [35] and static series [16, 17, 33] structures. Due to the state-space form of the model structure, augmentations can occur at the state and/or output level. We show a selection of possible state level augmentations in Table 1 and output level augmentations in Table 2. Here, static refers to augmentations that do not add new state dimensions beyond the baseline model states x_b . Dynamic augmentation structures [7, 20], on the other hand, add new augmentation states x_a to model missing dynamics. A broad range of further augmentations are possible. In this work, we restrict attention to the elementary augmentations listed in Tables 1 and 2, which will be discussed through this paper.

As discussed in the introduction, a general augmentation structure is desired. For this, a parameterisation of the operator \star is required, capable of characterising the intercon-

Table 1
Classes of state model augmentation structures.

static parallel (S-SP)	$x_{b,k+1} = f_{\text{base}}(x_{b,k}, u_k) + f_{\text{aug}}(x_{b,k}, u_k)$
static series output (S-SSO)	$x_{b,k+1} = f_{\text{aug}}(x_{b,k}, u_k, f_{\text{base}}(x_{b,k}, u_k))$
static series input (S-SSI)	$x_{b,k+1} = f_{\text{base}}(f_{\text{aug}}(x_{b,k}, u_k))$
dynamic parallel (S-DP)	$x_{b,k+1} = f_{\text{base}}(x_{b,k}, u_k) + f_{\text{aug}}(x_{b,k}, x_{a,k}, u_k)$ $x_{a,k+1} = g_{\text{aug}}(x_{b,k}, x_{a,k}, u_k)$
dynamic series output (S-DSO)	$x_{b,k+1} = f_{\text{aug}}(x_{b,k}, x_{a,k}, u_k, f_{\text{base}}(x_{b,k}, u_k))$ $x_{a,k+1} = g_{\text{aug}}(x_{b,k}, x_{a,k}, u_k)$
dynamic series input (S-DSI)	$x_{b,k+1} = f_{\text{base}}(f_{\text{aug}}(x_{b,k}, x_{a,k}, u_k))$ $x_{a,k+1} = g_{\text{aug}}(x_{b,k}, x_{a,k}, u_k)$

Table 2
Classes of output model augmentation structures.

static parallel (O-SP)	$\hat{y}_k = h_{\text{base}}(x_{b,k}, u_k) + h_{\text{aug}}(x_{b,k}, u_k)$
static series output (O-SSP)	$\hat{y}_k = h_{\text{aug}}(x_{b,k}, u_k, h_{\text{base}}(x_{b,k}, u_k))$
static series input (O-SSI)	$\hat{y}_k = h_{\text{base}}(h_{\text{aug}}(x_{b,k}, u_k))$
dynamic parallel (O-DP)	$\hat{y}_k = h_{\text{base}}(x_{b,k}, u_k) + h_{\text{aug}}(x_{b,k}, x_{a,k}, u_k)$ $x_{a,k+1} = g_{\text{aug}}(x_{b,k}, x_{a,k}, u_k)$
dynamic series output (O-DSO)	$\hat{y}_k = h_{\text{aug}}(x_{b,k}, x_{a,k}, u_k, h_{\text{base}}(x_{b,k}, u_k))$ $x_{a,k+1} = g_{\text{aug}}(x_{b,k}, x_{a,k}, u_k)$
dynamic series input (O-DSI)	$\hat{y}_k = h_{\text{base}}(h_{\text{aug}}(x_{b,k}, x_{a,k}, u_k))$ $x_{a,k+1} = g_{\text{aug}}(x_{b,k}, x_{a,k}, u_k)$

nection between the baseline model and the learning components. This would realise a fully parameterised general augmentation structure of (3). Additionally, an identification algorithm able to estimate the parameters of this general model augmentation structure is proposed, under the restriction that the model is well-posed.

3 LFR-based augmentation structure

In this section, we formulate a general representation of (3) in an LFR-based augmentation structure. Next, we derive the graph based representation of the proposed model structure, which is to be used to introduce sparsity to the LFR-based augmentation structure as well as for deriving conditions for well-posedness in Section 4. Finally, we introduce the parameterisation of the learning component that we will use to formulate our augmentation approach.

3.1 General LFR-based augmentation structure

As discussed in Section 2, many model augmentation structures are available in the literature, and now we propose a

unified structure based on the *Linear Fractional Representation* (LFR) that can represent all augmentation arrangements. The flexibility of this representation has made it popular in the field of robust control [40] and linear parameter-varying-control [37]. Furthermore, an LFR can also include nonlinear components in the interconnections [38], which has made LFRs useful for black-box nonlinear system representations [32, 34] and implicit learning [12]. Recent results have also shown that stability properties can be enforced on these black-box LFRs in a constraint-free manner at the cost of some representation capability [15, 29].

Introduce the following notation for the baseline terms:

$$\phi_{\text{base}}(\theta_{\text{base}}, z_{b,k}) = \begin{bmatrix} f_{\text{base}}(\theta_{\text{base}}, z_{b,k}) \\ h_{\text{base}}(\theta_{\text{base}}, z_{b,k}) \end{bmatrix}. \quad (4)$$

Moreover, we denote the learning component as ϕ_{aug} , which can be represented by any universal function approximator. We assume that it is implemented as a function with $\theta_{\text{aug}} \in \mathbb{R}^{n_{\theta_{\text{aug}}}}$ collecting its parameters. Latent variables $w_{b,k} \in \mathbb{R}^{n_{w_b} + n_y}$, $w_{a,k} \in \mathbb{R}^{n_{w_a}}$, $z_{a,k} \in \mathbb{R}^{n_{z_a}}$, and $z_{b,k} \in \mathbb{R}^{n_{z_b} + n_u}$ are introduced, and expressed as

$$\begin{bmatrix} z_{b,k} \\ z_{a,k} \end{bmatrix} = \begin{bmatrix} C_z^b \\ C_z^a \end{bmatrix} \hat{x}_k + \begin{bmatrix} D_{zu}^b \\ D_{zu}^a \end{bmatrix} u_k + \underbrace{\begin{bmatrix} D_{zw}^{bb} & D_{zw}^{ba} \\ D_{zw}^{ab} & D_{zw}^{aa} \end{bmatrix}}_{D_{zw}} \begin{bmatrix} w_{b,k} \\ w_{a,k} \end{bmatrix}, \quad (5)$$

where C_z^b , C_z^a , ..., D_{zw}^a are real matrices with dimensions compatible with the signal dimensions, and their elements are parameters that are optimised during model learning. The state transition and output equations are expressed as

$$\begin{bmatrix} x_{b,k+1} \\ x_{a,k+1} \end{bmatrix} = \underbrace{\begin{bmatrix} A^{bb} & A^{ba} \\ A^{ab} & A^{aa} \end{bmatrix}}_A \begin{bmatrix} x_{b,k} \\ x_{a,k} \end{bmatrix} + \underbrace{\begin{bmatrix} B_u^b \\ B_u^a \end{bmatrix}}_{B_u} u_k + \underbrace{\begin{bmatrix} B_w^{bb} & B_w^{ba} \\ B_w^{ab} & B_w^{aa} \end{bmatrix}}_{B_w} \begin{bmatrix} w_{b,k} \\ w_{a,k} \end{bmatrix},$$

$$\hat{y}_k = \underbrace{\begin{bmatrix} C_y^b & C_y^a \end{bmatrix}}_{C_y} \hat{x}_k + D_{yu} u_k + \begin{bmatrix} D_{yw}^b & D_{yw}^a \end{bmatrix} w_k,$$

where A , B_u , C_y , and D_{yu} are real matrices with appropriate signal dimensions representing the linear parts of the unmodeled dynamics, the baseline part participates in the relation through matrices B_w^b and D_{yw}^b , while the nonlinear black-box terms effect the dynamics through B_w^a and D_{yw}^a .

Finally, the LFR-based model augmentation structure (shown in Fig. 2) can be expressed in a compact form, as

$$\begin{bmatrix} \hat{x}_{k+1} \\ \hat{y}_k \\ z_{b,k} \\ z_{a,k} \end{bmatrix} = \underbrace{\begin{bmatrix} A & B_u & B_w^b & B_w^a \\ C_y & D_{yu} & D_{yw}^b & D_{yw}^a \\ C_z^b & D_{zu}^b & D_{zw}^{bb} & D_{zw}^{ba} \\ C_z^a & D_{zu}^a & D_{zw}^{ab} & D_{zw}^{aa} \end{bmatrix}}_{W(\theta_{\text{LFR}})} \begin{bmatrix} \hat{x}_k \\ u_k \\ w_{b,k} \\ w_{a,k} \end{bmatrix}, \quad (6a)$$

$$w_{b,k} = \phi_{\text{base}}(\theta_{\text{base}}, z_{b,k}), \quad (6b)$$

$$w_{a,k} = \phi_{\text{aug}}(\theta_{\text{aug}}, z_{a,k}), \quad (6c)$$

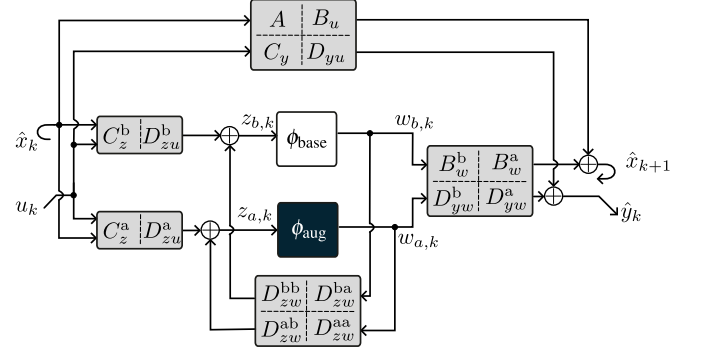


Fig. 2. LFR-based augmentation structure of the baseline model characterised by ϕ_{base} with learning components ϕ_{aug} .

where W is the LFR matrix, and all parameters determining the matrices A , B_u , ..., D_{zw}^a are collected into θ_{LFR} . Since θ_{LFR} is included in the (tunable) model parameters, the final interconnection structure of the LFR-based augmentation is formed throughout model learning, hence the flexibility of the approach. However, an inherent challenge of LFR model structures is ensuring well-posedness of the model structure. As the model structure allows algebraic loops, it is possible to retrieve ill-posed realisations. We define the *well-posedness* (WP) property as

Property 1 (Well-posedness) For any value of $\hat{x}_k \in \mathbb{R}^{n_x}$ and $u_k \in \mathbb{R}^{n_u}$, the signal relations in (6) admit a unique solution $z_k = [z_{b,k}^\top \ z_{a,k}^\top]^\top$.

Conditions to ensure the well-posedness are introduced in Section 4. The unified representation capability of the proposed LFR structure is shown by the following theorem.

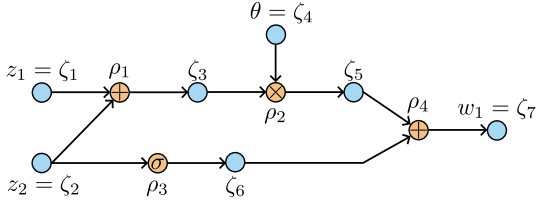
Theorem 2 (Unified representation) Given a baseline model (2) with parameters θ_{base} connected to learning components f_{aug} , g_{aug} and h_{aug} , each parametrised with θ_{aug} , in terms of (3), where the operator \star corresponds to any of the interconnections listed in Table 1 and 2. Then, for the considered model structure (6), there exists a $\theta_{\text{LFR}} \in \mathbb{R}^{n_{\theta_{\text{LFR}}}}$ and choices of latent dimensions $n_{w_a}, n_{z_a} \geq 0$ and a ϕ_{aug} function, such that (3) and (6) are equivalent representations of the same dynamic behaviour.

PROOF. See Appendix A. ■

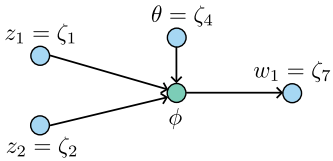
3.2 Computational graph of the interconnection

The full parameterisation of W in the proposed LFR-based model augmentation structure gives a general representation of (3). However, due to full parameterisation, the actual interconnection of the learning and baseline model components is represented in a black-box fashion compared to the cases listed in Tables 1 and 2.

To be able to detect or even enforce a particular configuration of these components, we investigate the computational graph of the augmentation interconnection (3). This graph makes clear what each edge, i.e., element of θ_{LFR} , does in the augmentation structure, and thus also what removing it for sparsification will do. Additionally, the graph representation



(a) Full computational graph



(b) Computational graph with subgraph ϕ

Fig. 3. Computational graph representation of the function $w_1 = \phi(\theta, z_1, z_2) = (z_1 + z_2)\theta + \sigma(z_2)$.

will provide general conditions on the well-posedness of the proposed model structure in Section 4.

First, we introduce computational graphs, then present the graph representations of the baseline model and the learning component, which are finally combined into the LFR model graph. Here we make use of the following graph notions: $G = (V, E)$ is a graph with nodes V and edges E , \deg^+ is the indegree of a node, \deg^- is the outdegree of a node, $\text{disjoint}(V, W)$ is the disjoint union of set between two sets V and W defined as $V \cup W$ with $V \cap W = \emptyset$, source(W) defines a set of nodes $V = \{v \in W \mid \deg^-(v) = 0\}$, and sink(W) defines a set of nodes $V = \{v \in W \mid \deg^+(v) = 0\}$. We also introduce the shorthand notation $\text{outvar}(V, W)$ to define the set of edges $E_{vw} = \{(v, w) \mid v \in V, w \in W, \deg^+(v) = \deg^-(w) = 1\}$, and $G_c = (V_c, E_c) = G \setminus V_s$ for vertex contraction with $G = (V, E)$, $V_s \subset V$, $V_c = V \setminus V_s \cup v_c$ and v_c being the contracted vertex.

3.2.1 Computational graphs

We take the formulation of the *computational graph* as defined in [3]. First, take the *computational problem* defined as the set of M functions

$$w_i = \phi_i = (z_1, \dots, z_K), \quad i = 1, \dots, M, \quad (7)$$

of K real variables $z_1, \dots, z_K \in \mathbb{R}$ from which M real quantities $w_i \in \mathbb{R}$ are obtained. Each function $\phi_i : \mathbb{R}^K \rightarrow \mathbb{R}$ can be described by a *computational process* consisting of a number of primitive operators

$$\zeta_{i_c,0} := \rho_c(\zeta_{i_c,1}, \dots, \zeta_{i_c,s}), \quad c = 1, \dots, L \quad (8)$$

where the values $\zeta_{i_c,j} \in \mathbb{R}$ and $\rho_c : \mathbb{R}^s \rightarrow \mathbb{R}$. For all $j \in [1, \dots, s]$, $\zeta_{i_c,j} \in [z_1, \dots, z_K, \zeta_{i_b,0}]$ with $b < c$, i.e., the inputs to ρ_c can be the input of ϕ_i or output from a previous operator ρ_b . For $j = 0$, $\zeta_{i_c,0} \in [w_1, \dots, w_M, \zeta_{i_b,1}, \dots, \zeta_{i_b,s}]$ with $b > c$, i.e., the output of ρ_c can be the output of ϕ_i or input to a next operator ρ_b . We consider primitive operators $\rho_c : \mathbb{R}^s \rightarrow \mathbb{R}$, with $s \in \{1, 2\}$, to be either: addition, multiplication or a nonlinear injective function (where $s = 1$).

The *computational process* defines and it is characterised by a *computational graph*, where both ρ_c and $\zeta_{i_c,j}$ are nodes in the graph. This computational graph is defined as follows:

Definition 3 (Computational graph) A directed graph denoted by $G = (V, E)$ with $V = \text{disjoint}(V_\zeta, V_\rho)$ the set of vertices and $E = \text{disjoint}(E_{\zeta\rho}, E_{\rho\zeta})$ the set of edges is called a computational graph if

- (a) $V_\rho = \{\rho_1, \dots, \rho_L\}$, $V_\zeta = \{\zeta_1, \dots, \zeta_K\}$
- (b) $V_z = \text{source}(V_\zeta)$, $V_w = \text{sink}(V_\zeta)$
- (c) $E_{\zeta\rho} = \{(\rho, \zeta) \mid \rho \in V_\rho, \zeta \in V_\zeta \text{ and } \frac{\partial \rho}{\partial \zeta} \neq 0\}$
- (d) $E_{\rho\zeta} = \text{outvar}(V_\rho, V_\zeta \setminus V_z)$

(a) defines the sets of operator and variable nodes respectively. (b) defines subsets of the variables representing the inputs and outputs respectively (i.e., sources and sinks in graph nomenclature). Lastly, (c) defines what variable nodes are inputs to which operators, and (d) defines the connection of the output variables for each operator. In Fig. 3a we show the computational graph for the example function $w_1 = \phi(\theta, z_1, z_2) = (z_1 + z_2)\theta + \sigma(z_2)$.

By defining a subgraph G_{ϕ_i} , we can formulate a more compact notation. The computational subgraph G_{ϕ_i} contains the nodes $V_{\phi_i} = (V_{\zeta_i} \cup V_{\rho_i}) \setminus V_{w_i} \setminus V_{z_i}$ and the edges internal to these nodes. Then by vertex contraction $G \setminus V_{\phi_i}$ we get the contracted noted v_{ϕ_i} that represents the multivariate function ϕ_i in (7). Such a contracted node v_{ϕ_i} is shown for the example function in Fig. 3b. For each function ϕ_i in the computational problem, a computational graph G_{ϕ_i} can be defined. By taking the union of these graphs as

$$G_\phi = (V_\phi, E_\phi) = (V_{\phi_1} \cup \dots \cup V_{\phi_M}, E_{\phi_1} \cup \dots \cup E_{\phi_M}) \quad (9)$$

we obtain the computational graph G_ϕ of the entire computational problem (7) with K inputs and M outputs, as visualised in Fig. 5. Note that due to the union, nodes and edges may be shared between the computational graphs G_{ϕ_i} .

3.2.2 Graph of baseline model

The baseline model (2) can be represented with a computational graph as

$$\begin{bmatrix} w_{b,1} \\ \vdots \\ w_{b,n_{x_b}} \\ w_{b,n_{x_b}+1} \\ \vdots \\ w_{b,n_{x_b}+n_y} \end{bmatrix} = \begin{bmatrix} \phi_{\text{base}_1}(\theta_{\text{base},1}, z_{b,k,1}) \\ \vdots \\ \phi_{\text{base}_{n_{x_b}}}(\theta_{\text{base},n_{x_b}}, z_{b,k,n_{x_b}}) \\ \phi_{\text{base}_{n_{x_b}+1}}(\theta_{\text{base},n_{x_b}+1}, z_{b,k,n_{x_b}+1}) \\ \vdots \\ \phi_{\text{base}_{n_{x_b}+n_y}}(\theta_{\text{base},n_{x_b}+n_y}, z_{b,k,n_{x_b}+n_y}) \end{bmatrix} = \begin{bmatrix} f_{\text{base}}(\theta_{\text{base}}, z_{b,k}) \\ h_{\text{base}}(\theta_{\text{base}}, z_{b,k}) \end{bmatrix}, \quad (10)$$

where we describe $z_{b,k} = \text{vec}(x_{b,k}, u_k)$ and θ_{base} as input variables, $w_{b,k} = \text{vec}(x_{b,k+1}, \hat{y}_k)$ as output variables, and $\theta_{\text{base},1}, \dots, \theta_{\text{base},n_{x_b}+n_y} \in \theta_{\text{base}}$ as the parameters (i.e., the

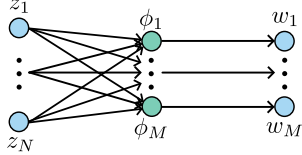


Fig. 4. Computational graph for a computation problem consisting of M functions $\phi_1 \dots \phi_M$.

parameters may be shared between functions ϕ_{base_i} , and similarly $z_{b,k,1}, \dots, z_{b,k,n_{x_b}+n_y} \in V_{z_b}$.

Which subset of θ_{base} and $z_{b,k}$ are input to each function ϕ_{base_i} , which follows from the baseline model (2) considered. After deriving a computational graph $G_{\phi_{\text{base}_i}}$ for each function $\phi_{\text{base}_1}, \dots, \phi_{\text{base}_{n_{x_b}+n_y}}$, the computational graph $G_{\phi_{\text{base}}}$ is derived by the graph union as in (9), with the resulting nodes V_{z_b} , V_{w_b} and $V_{\phi_{\text{base}}}$. Notably, $E_{z_b \phi_{\text{base}}}$ is sparse, e.g., the number of edges between V_{z_b} and $V_{\phi_{\text{base}}}$ is smaller than would be permissible by any arbitrary chosen baseline model (2).

3.2.3 Graph of the learning component

Similarly as for the baseline model, we describe the learning function graph for the computational problem as

$$\begin{bmatrix} w_1 \\ \vdots \\ w_{n_{w_a}} \end{bmatrix} = \begin{bmatrix} \phi_{\text{aug}_1}(\theta_{\text{aug},1}, z_{a,k,1}) \\ \vdots \\ \phi_{\text{aug}_{n_{w_a}}}(\theta_{\text{aug},n_{w_a}}, z_{a,k,n_{w_a}}) \end{bmatrix} = \phi_{\text{aug}}(\theta_{\text{aug}}, z_{a,k}),$$

Then the computational graph $G_{\phi_{\text{aug}}}$ is derived as before, with the resulting nodes V_{z_a} , V_{w_a} and $V_{\phi_{\text{aug}}}$.

3.2.4 LFR model graph

With the baseline model graph $G_{\phi_{\text{base}}}$ and the learning component graph $G_{\phi_{\text{aug}}}$, we can define the interconnection structure between these graphs and the signals \hat{x}_k , u_k , \hat{x}_{k+1} and \hat{y}_k of the model. For ease of notation, we will leave out the θ nodes, as these are not altered any further. We start by defining how the model signals are matched to $G_{\phi_{\text{base}}}$ and $G_{\phi_{\text{aug}}}$, by taking the following parameterised summation

$$\zeta = \sum_{i=1}^{\deg^-(\zeta)} \theta_i v_i, \quad (11)$$

where $\zeta \in \text{disjoint}(V_{x^+}, V_y, V_{z_b}, V_{z_a})$ and $v_i \in \text{disjoint}(V_x, V_u, V_{w_b}, V_{w_a})$ and θ_i is the weight of the summation. These summation operations are then represented by the summation nodes V_ζ . Then the interconnect graph can be defined as

Definition 4 (Interconnection graph) The computational graph of the interconnection between $G_{\phi_{\text{base}}}$ and $G_{\phi_{\text{aug}}}$ is a directed graph denoted by $G_{\text{LFR}} = (V_{\text{LFR}}, E_{\text{LFR}})$, where $V_{\text{LFR}} = \text{disjoint}(V_{x^+}, V_y, V_{z_b}, V_{z_a}, V_x, V_u, V_{w_b}, V_{w_a})$ and $E_{\text{LFR}} = \text{disjoint}(E_{\zeta_b z_b}, E_{\zeta_a z_a}, E_{\zeta_x x^+}, E_{\zeta_y y}, E_{\phi_{\text{base}}}, E_{\phi_{\text{aug}}})$

- (a) $V_{\zeta_b} = \{\zeta_1, \dots, \zeta_{n_{z_b}}\}$, $V_{\zeta_a} = \{\zeta_1, \dots, \zeta_{n_{z_a}}\}$,
 $V_{\zeta_x} = \{\zeta_1, \dots, \zeta_{n_x}\}$, $V_{\zeta_y} = \{\zeta_1, \dots, \zeta_{n_y}\}$

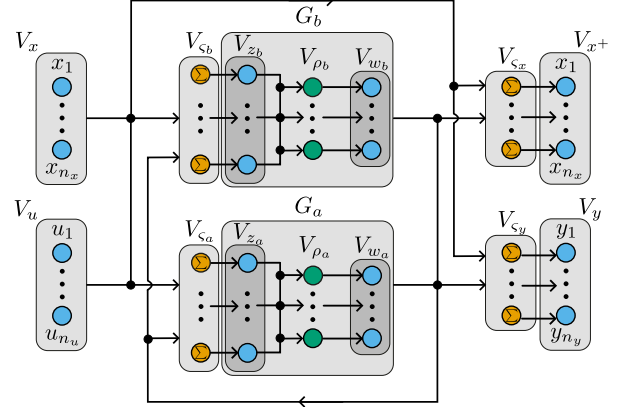


Fig. 5. Computational graph of the interconnection of G_b and G_a .

- (b) $E_{\zeta_b z_b} = \text{outvar}(V_{\zeta_b}, V_{z_b})$, $E_{\zeta_a z_a} = \text{outvar}(V_{\zeta_a}, V_{z_a})$,
 $E_{\zeta_x x^+} = \text{outvar}(V_{\zeta_x}, V_{x^+})$, $E_{\zeta_y y} = \text{outvar}(V_{\zeta_y}, V_y)$
(c) $\forall v \in V_x \cup V_u, \deg^-(v) = 0$, $\forall v \in V_{x^+} \cup V_y, \deg^+(v) = 0$
(d) $E_{v\zeta} = \{(v, \zeta) | v \in \text{disjoint}(V_{z_b}, V_{z_a}, V_{x_k}, V_{u_k}), \zeta \in V_\zeta\}$

(a) defines the summation nodes for the baseline, augmentation, state, and output nodes and (b) defines the one-to-one outgoing edges from these summation nodes to the respective output nodes ρ . (c) defines existing nodes as inputs and outputs respectively (i.e., sources and sinks). Finally, (d) defines the edges between the state, input, baseline, and augmentation and the summation nodes.

By applying vertex contraction with the nodes $\zeta_i \in V_\zeta$ and the nodes to which the corresponding outgoing edge of ζ leads, either V_z , V_{x^+} or V_y , on G_{LFR} , and also applying vertex contraction with node sets V_{ρ_b} and V_{ρ_a} on G_{LFR} , we retrieve a graph with only the variable nodes. Considering P_i to be the adjacency matrix for the edge set E_i , then the adjacency matrix for the interconnected graph is

$$P = \begin{bmatrix} \hat{x}_k & u_k & z_b & z_a & w_b & w_a & \hat{x}_{k+1} & \hat{y}_k \\ \hat{x}_k & 0 & 0 & 0 & 0 & 0 & 0 & 0 \\ u_k & 0 & 0 & 0 & 0 & 0 & 0 & 0 \\ z_b & P_{z_b x} & P_{z_b u} & 0 & 0 & P_{z_b w_b} & P_{z_b w_a} & 0 & 0 \\ z_a & P_{z_a x} & P_{z_a u} & 0 & 0 & P_{z_a w_b} & P_{z_a w_a} & 0 & 0 \\ w_b & 0 & 0 & P_b & 0 & 0 & 0 & 0 & 0 \\ w_a & 0 & 0 & 0 & P_a & 0 & 0 & 0 & 0 \\ \hat{x}_{k+1} & P_{xx} & P_{xu} & 0 & 0 & P_{xw_b} & P_{xw_a} & 0 & 0 \\ \hat{y}_k & P_{yx} & P_{yu} & 0 & 0 & P_{yw_b} & P_{yw_a} & 0 & 0 \end{bmatrix}. \quad (12)$$

By considering all edge sets maximal, i.e., fully connected where allowed, the summations in (11) recover the proposed LFR structure (6). The augmentation structures in Tables 1 and 2 correspond to sparse adjacency matrices. Thus, we can enforce or detect these augmentation structures by these sparse patterns in the adjacency matrix.

3.3 Parametrisation of the learning component

The proposed LFR-based augmentation structure allows for the use of any parameterised learning function ϕ_{aug} without loss of generality. For the remainder of this report, however, we will consider ϕ_{aug} to be parameterised by an ANN. An ANN with q hidden layers, each composed of m_i neurons and activation function $\rho : \mathbb{R} \rightarrow \mathbb{R}$, is defined as

$$\xi_{i,j} = \rho \left(\sum_{l=1}^{m_{i-1}} \theta_{w,i,j,l} \xi_{i-1,l} + \theta_{b,i,j} \right) \quad (13)$$

where $\xi_i = \text{col}(\xi_{i,1}, \dots, \xi_{i,m_i})$ is the latent variable representing the output of layer $1 \leq i \leq q$, $\theta_{w,i,j,l}$ and $\theta_{b,i,j}$ are the weight and bias parameters of the network. Here, $\text{col}(\cdot)$ denotes the composition of a column vector. For a ϕ_{aug} with q hidden layers and linear input and output layers, this gives

$$\phi_{\text{aug}}(\theta_{\text{aug}}, z_{a,k}) = \theta_{w,q+1} \xi_q(k) + \theta_{b,q+1} \quad (14a)$$

$$\xi_0(k) = z_{a,k} \quad (14b)$$

This can be extended to residual neural network (ResNet) [19], which adds a linear bypass given as

$$\phi_{\text{aug}}(\theta_{\text{aug}}, z_{a,k}) = \theta_{w,q+1} \xi_q(k) + \theta_{b,q+1} + W_a z_{a,k} \quad (15a)$$

$$\xi_0(k) = z_{a,k} \quad (15b)$$

where W is a parameterised residual weight matrix of appropriate dimensions. The additional linear bypass can capture unknown linear dynamics in the learning functions. This is preferable over capturing these dynamics through nonlinear activation functions, since this is more likely to extrapolate better and has shown better learning performance in similar settings [31]. It additionally allows for stable initialisations of the proposed LFR structure as discussed in Section 5.4.

This finalises the structure of the fully parameterised general augmentation structure of (3). We continue with providing well-posedness conditions and an identification algorithm.

4 LFR structure well-posedness

We now propose conditions under which Property 1 is guaranteed. To derive conditions, we rewrite (5) into

$$\underbrace{\begin{bmatrix} z_{b,k} \\ z_{a,k} \end{bmatrix}}_{v(z_{b,k}, z_{a,k})} - D_{zw} \phi(z_{b,k}, z_{a,k}) = \begin{bmatrix} C_z^b & D_{zu}^b \\ C_z^a & D_{zu}^a \end{bmatrix} \begin{bmatrix} \hat{x}_k \\ u_k \end{bmatrix}, \quad (16)$$

where $\text{col}(\phi_{\text{base}}(\theta_{\text{base}}, z_{b,k}), \phi_{\text{aug}}(\theta_{\text{aug}}, z_{a,k})) = \phi(z_{b,k}, z_{a,k})$. Then, if the inverse $v^{-1}(z_{b,k}, z_{a,k})$ exists,

$$\begin{bmatrix} z_{b,k} \\ z_{a,k} \end{bmatrix} = v^{-1} \left(\begin{bmatrix} C_z^b & D_{zu}^b \\ C_z^a & D_{zu}^a \end{bmatrix} \begin{bmatrix} \hat{x}_k \\ u_k \end{bmatrix} \right). \quad (17)$$

Substitution into (6a) then eliminates (6b) and (6c). The existence of the inverse $v^{-1}(z_{b,k}, z_{a,k})$ can be guaranteed by the following theorem. For this, we introduce the notation C^n to denote the class of functions whose derivatives up to order n exist and are continuous.

Theorem 5 (Hadamard's global inverse function [23])

Let the function $v(z) : \mathbb{R}^N \rightarrow \mathbb{R}^N$ be a C^2 mapping. Suppose that the determinant of the Jacobian $\det(Dv(z)) \neq 0, \forall z \in \mathbb{R}^N$. In addition, suppose that $v(z)$ is proper, i.e., $\|v(z)\|_2^2 \rightarrow \infty$ as $\|z\|_2^2 \rightarrow \infty$. Then, there exists an inverse function $v^{-1}(z)$ such that $v(v^{-1}(z)) = z$ and $v^{-1}(v(z)) = z$.

The conditions of this theorem can be met through a variety of parameterisations of the interconnect matrix and the functions $\phi_i(z_i)$ [29, 39]. We prove that the conditions of the theorem can be met by the following conditions on the computational graph G_{LFR} and the functions ϕ_{base} and ϕ_{aug} .

Condition 6 (Directed acyclic graph) The computational graph G_{LFR} is acyclic, i.e., it contains no cycles.

Remark 7 For a given adjacency matrix P , the presence of a topological ordering, and thus the acyclic property, can be computed in linear time $\mathcal{O}(n)$ [2].

Condition 8 (Differentiability) The functions ϕ_{base} and ϕ_{aug} are C^2 .

Under these conditions, the following theorem holds:

Theorem 9 (Well-posedness of the augmentation) Given a parameterisation $\theta = (\theta_{\text{LFR}}, \theta_{\text{base}}, \theta_{\text{aug}})$ of the model augmentation structure (6), the parameterised structured is well-posed if Conditions 6 and 8 hold.

PROOF. By Condition 8, ϕ_{base} and ϕ_{aug} are C^2 , and also

$$v(z_{b,k}, z_{a,k}) = \begin{bmatrix} z_{b,k} \\ z_{a,k} \end{bmatrix} + D_{zw} \begin{bmatrix} \phi_{\text{base}}(\theta_{\text{base}}, z_{b,k}) \\ \phi_{\text{aug}}(\theta_{\text{aug}}, z_{a,k}) \end{bmatrix} \quad (18)$$

is C^2 . This satisfies the first condition of Hadamard's global inverse function theorem.

Second, the properness of $v(z_{b,k}, z_{a,k})$. By Condition 6, we can, by elementary row and column operations, retrieve a strict lower triangular of $D_{zw} D \phi(z)$. This implies that the function $\bar{\phi}(z) = D_{zw} \phi(z)$ has without loss of generality, the structure

$$\bar{\phi}_i(z) = \bar{\phi}_i(z_1, \dots, z_{i-1}), \quad i = 1, \dots, n_z,$$

with $\bar{\phi}(z) = \text{col}(\bar{\phi}_1, \dots, \bar{\phi}_{n_z})$. Each component of v is given by

$$v_i(z) = z_i + \bar{\phi}_i(z_1, \dots, z_{i-1}), \quad i = 1, \dots, n_z. \quad (19)$$

We then prove that $\|v(z)\|_2^2 \rightarrow \infty$ as $\|z\|_2^2 \rightarrow \infty$. From $\|z\|_2^2 \rightarrow \infty$, we have that at least one $|z_i| \rightarrow \infty$ while the remainder may remain bounded. We thus prove that this z_i induces $\|v(z)\|_2^2 \rightarrow \infty$. For $i = 1$, $\bar{\phi}_1(z)$ is constant, therefore, $v_1(z) = z_1 + c_1$ for some constant $c_1 \in \mathbb{R}$. Then $|v_1(z)| \rightarrow \infty$ as $|z_1| \rightarrow \infty$. For $i = 2, \dots, n_z$, if $\bar{\phi}_i$ is bounded, then by (19) $|v_i(z)| \rightarrow \infty$ as $|z_i| \rightarrow \infty$. Thus if any $|z_i| \rightarrow \infty$, and thus $\|z\|_2^2 \rightarrow \infty$, then $\|v(z)\|_2^2$.

Third, we prove the Jacobian determinant condition. The Jacobian determinant of $v(z_{b,k}, z_{a,k})$ is written as

$$\det(Dv(z_{b,k}, z_{a,k})) = \det(I - D_{zw} D \phi(z_{b,k}, z_{a,k})). \quad (20)$$

By Condition 6, we know that all subgraphs of G_{LFR} are acyclic. Thus the feedback connection, given as

$D_{zw}\text{diag}(P_b, P_a)$, must be acyclic and thus nilpotent. Then, by the construction of P_b and P_a , also the matrix $D_{zw}\text{diag}(D\phi_{\text{base}}, D\phi_{\text{aug}})$ is nilpotent, implying

$$\det \left(\mathbf{I} - D_{zw} \begin{bmatrix} D\phi_{\text{base}} & 0 \\ 0 & D\phi_{\text{aug}} \end{bmatrix} \right) \neq 0. \quad (21)$$

Then $v(z_{b,k}, z_{a,k})$ has an inverse v^{-1} and the algebraic loop can be eliminated, proving the well-posedness of (6). ■

Remark 10 Condition 6, which ensures the well-posedness of the LFR-based structure in (6), can be satisfied through several strategies. The simplest approach is to restrict $D_{zw} \equiv 0$ during model training. However, this constraint limits the generality of the method by reducing the variety of model augmentation structures that the LFR-based representation can capture. A more flexible alternative is to include only one of the components, either D_{zw}^{ba} or D_{zw}^{ab} , in the parameter vector θ_{LFR} , while setting all other elements of D_{zw} to zero. This approach preserves the acyclic condition while allowing for a richer class of model augmentation structures to be represented by the LFR-based formulation. The selection between tuning D_{zw}^{ba} or D_{zw}^{ab} is a modelling choice and should be guided by prior physical insights. It is left to future work to develop parameterisations that directly guarantee well-posedness of the model structure.

5 Identification Algorithm

Given the proposed model augmentation structure (6), our goal is to estimate the parameters of the model structure based on measured data in order to capture the behaviour of the data-generating system (1). To this end, we specify an identification algorithm consisting of identification criterion, baseline parameter regularisation, data and baseline model normalisation, and parameter initialisation.

5.1 Truncated loss function

We adapt the multiple-shooting-based truncated objective function [5]. This is a truncated prediction loss based objective function. The data \mathcal{D}_N is split into N subsections of length T . This allows for the use of computationally efficient batch optimisation methods popular in machine learning, while also increasing data efficiency [5]. This truncated objective function is given as

$$V_{\text{trunc}}(\theta) = \frac{1}{N-T+1} \sum_{i=1}^{N-T+1} \frac{1}{T} \sum_{\ell=0}^{T-1} \|\hat{y}_{k_i+\ell|k_i} - y_{k_i+\ell}\|_2^2 \quad (22a)$$

$$\begin{bmatrix} \hat{x}_{k_i+\ell+1|k_i} \\ \hat{y}_{k_i+\ell|k_i} \\ w_{b,k_i+\ell|k_i} \\ w_{a,k_i+\ell|k_i} \end{bmatrix} := W(\theta_{\text{LFR}}) \begin{bmatrix} \hat{x}_{k_i+\ell|k_i} \\ u_{k_i+\ell} \\ z_{b,k_i+\ell|k_i} \\ z_{a,k_i+\ell|k_i} \end{bmatrix} \quad (22b)$$

$$w_{b,k_i+\ell|k_i} := \phi_{\text{base}}(\theta_{\text{base}}, z_{b,k}) \quad (22c)$$

$$w_{a,k_i+\ell|k_i} := \phi_{\text{aug}}(\theta_{\text{aug}}, z_{a,k}) \quad (22d)$$

$$\hat{x}_{k|k} := \psi(\theta_{\text{encoder}}, y_{k-n_a}^{k-1}, u_{k-n_b}^{k-1}), \quad (22e)$$

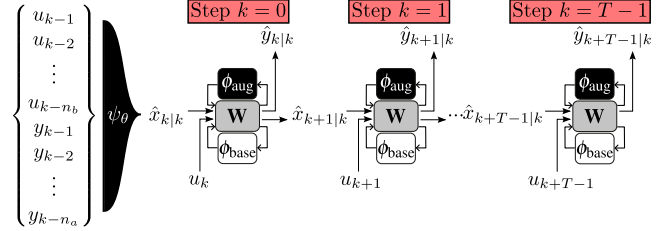


Fig. 6. SUBNET structure: the subspace encoder ψ_θ estimates the initial state at time k based on past inputs and outputs, then it is propagated through ϕ_θ multiple times until a simulation length T .

where $\theta = \text{col}(\theta_{\text{base}}, \theta_{\text{aug}}, \theta_{\text{LFR}}, \theta_{\text{encoder}})$ is the joint parameter vector, $k+\ell|k$ indicates the state \hat{x}_k or the output \hat{y}_k at time $k+\ell$ simulated from the initial state $\hat{x}_{k|k}$ at time k . The subsections start at a randomly selected time $k_i \in \{n+1, \dots, N-T\}$. The initial state of these subsections is estimated by an encoder function ψ using past input-output data, i.e., $\hat{x}_{k|k} = \psi(\theta_{\text{encoder}}, y_{k-n_a}^{k-1}, u_{k-n_b}^{k-1})$ where $u_{k-n_b}^{k-1} = [u_{k-n_b}^\top \dots u_{k-1}^\top]^\top$ for $\tau \geq 0$ and $y_{k-n_a}^{k-1}$ is defined similarly. The model structure with the encoder ψ included, is shown in Fig. 6.

The existence of the encoder ψ has been shown in [4] for state-space models. We give a brief overview of the underlying mechanism. We derive the n -step ahead predictor of the data generating system (1), resulting in

$$y_k^{n+k} = \begin{bmatrix} h(x_k, u_k) + e_k \\ (h \circ f)(x_k, u_k^{k+1}) + e_{k+1} \\ \vdots \\ (h \circ_n f)(x_k, u_k^{n+k}) + e_{k+n} \\ \Gamma_n(x_k, u_k^{n+k}) + e_k^{n+k} \end{bmatrix}. \quad (23)$$

where \circ_n stands for n times recursive function composition. If Γ_n is partially invertible as $x_k = \Phi_n(u_k^{n+k}, y_k^{n+k} - e_k^{n+k})$, then the reconstructability map [21] is given as

$$x_k = (\circ_n f)(x_{k-n}, u_{k-n}^k) \quad (24a)$$

$$= (\circ_n f)(\Phi_n(u_{k-n}^k, y_{k-n}^k - e_{k-n}^k), u_{k-n}^k) \quad (24b)$$

$$= \Psi_n(u_{k-n}^k, y_{k-n}^k - e_{k-n}^k). \quad (24c)$$

However, the noise sequence e_{k-n}^k is not available in practice. Under the assumption that e_k is i.i.d. white noise, we can use the conditional expectation of (24c) as an estimate of x_k :

$$\bar{x}_k = \mathbb{E}_{e_k} [x_k | u_{k-n}^k, y_{k-n}^k] = \bar{\Psi}(u_{k-n}^k, y_{k-n}^k), \quad (25)$$

which is an unbiased estimator of x_k [22]. This estimator is difficult to compute in practice due to the required analytical inversion to obtain Φ_n , which varies with the choices of θ_{base} , θ_{aug} and θ_{LFR} . Instead the parameterised function estimator ψ is used to co-estimate $\bar{\Psi}$ with $W(\theta_{\text{LFR}})$, ϕ_{base} and ϕ_{aug} .

5.2 Baseline parameter regularisation

The proposed LFR-based model structure (6) is overparameterised and, as a result, the optimal parameter values

$(\theta_{\text{base}}^*, \theta_{\text{aug}}^*, \theta_{\text{LFR}}^*)$ that minimise (22) are not unique. Therefore, the joint identification of all parameters can result in the learning components representing or cancelling out part of the baseline model dynamics. These non-unique parameterisations have similar model performance; however, some parameterisations may generate physical parameters that deviate wildly from the expected parameters, even leading to physically unrealistic parameter values. To address this issue and retain the interpretability of the baseline model, we adapt the regularisation cost term from [8, 9]:

$$V^{\text{reg}}(\theta) = \|\Lambda(\theta_{\text{base}} - \theta_{\text{base}}^0)\|_2^2 \quad (26)$$

where $\Lambda = \lambda \text{diag}(\theta_{\text{base}}^0)^{-1}$ with $\lambda \in \mathbb{R}_{\geq 0}$ as a tunable parameter. This regularisation term (26) penalises deviations of the baseline parameters from the a priori selected values θ_{base}^0 , with the diagonal element normalising the importance of the parameters compared to each other. The cost function with the regularisation term becomes

$$V_{\mathcal{D}_N}(\theta) = V_{\mathcal{D}_N}^{\text{trunc}}(\theta) + V^{\text{reg}}(\theta). \quad (27)$$

The tunable variable λ determines how much the baseline parameters can deviate from the nominal parameter set θ_{base}^0 , relative to the change in T -step-ahead prediction cost (22).

5.3 Data and baseline model normalisation

For the estimation of model structures containing ANNs, normalisation of the input and output data to zero mean and to a standard deviation of 1 has been shown to improve model estimation [6]. Therefore, we normalise u and y in \mathcal{D}_N and aim to initialise the model structure and (6) so that \hat{x} is also normalised as in [5]. For this, the to-be-augmented baseline model ϕ_{base} needs to be considered in the normalisation process. We take ϕ_{base} into consideration based on the work in [32]. This results in a model that takes normalised input and state, and returns a normalised output while not altering its dynamics. For a baseline model operating around zero mean \hat{x} , u , \hat{y} , this can be achieved by the transformation

$$\bar{f}_{\text{base}} = T_x f_{\text{base}}(\theta_{\text{base}}, T_x^{-1} x_b, T_u^{-1} u) \quad (28a)$$

$$\bar{h}_{\text{base}} = T_y h_{\text{base}}(\theta_{\text{base}}, T_x^{-1} x_b, T_u^{-1} u), \quad (28b)$$

where $T_u \in \mathbb{R}^{n_u}$ is a diagonal matrix composed as $T_u^{-1} = \text{diag}(\sigma_{u_1}^{-1}, \dots, \sigma_{u_{n_u}}^{-1})$, where σ_u is the sample-based standard deviation of each input signal, computed based on the data set \mathcal{D}_N . The transformation matrix T_y is defined in a similar way. For T_x , the standard deviation σ_x is determined on a sequence of baseline states x_b . For this, we simulate the baseline model with θ_{base}^0 for the given input sequence resulting in $\hat{x}_{b,k}$. We define an extended data set $\hat{\mathcal{D}}_N = \{(y_k, \hat{x}_{b,k}, u_k)\}_{k=1}^N$ for initialisation of the encoder later.

5.4 Model structure initialisation

Next, we consider the initialisation of the learning components, LFR matrix, and the encoder. A common approach in the literature for initialising ANNs is to randomly assign weights and biases. However, for baseline models, random initialisation can be unstable and result in poor optimisation

results. Furthermore, initialisation based on prior information, e.g., baseline model behaviour, can improve convergence rate and enhance model accuracy.

5.4.1 Model behaviour at initialisation

We propose to initialise the parameters θ so that the LFR-based model structure with the encoder behaves equivalent to the baseline model on initialisation. We note the model structure (6) with $z_{b,k}$ and $z_{a,k}$ eliminated as Ω . Then the initialisation of θ should realise the following behaviour

$$\begin{bmatrix} x_{b,k+1} \\ x_{a,k+1} \\ \hat{y}_k \end{bmatrix} = \Omega(\theta, z_{b,k}, z_{a,k}) = \begin{bmatrix} f_{\text{base}}(\theta_{\text{base}}^0, z_{b,k}) \\ \phi_{\text{aug}}(\theta_{\text{aug}}^0, z_{a,k}) \\ h_{\text{base}}(\theta_{\text{base}}^0, z_{b,k}) \end{bmatrix}, \quad (29)$$

where θ_{aug}^0 are the initialised parameters for the augmentation. It is not trivial to determine such an initialisation for any arbitrary baseline model, learning function, and LFR matrix combination. We propose here a method that can achieve this initialisation under the following conditions:

- (a) The computational graph G_{LFR} is acyclic
- (b) The learning functions are ResNets (15).

Condition (a) is the same condition as for the well-posedness proof and thus is not restrictive. Condition (b) is required to feasibly create series augmentations that can have baseline model behaviour.

5.4.2 Encoder initialisation

The encoder is parameterised by an ANN, e.g., a ResNET. To guarantee baseline behaviour at initialisation, this encoder should at initialisation output the baseline state sequence as in the extended dataset $\hat{\mathcal{D}}_N$. This could be derived analytically as in Section 5.1, but this is complicated on not feasible for all ANNs. Instead, we consider a data-driven approach. We fit a baseline encoder ψ_{base} on this dataset using the following loss function during the initialisation step

$$V_{\text{enc}}(\theta) = \frac{1}{N} \sum_{k=1}^N \left\| \psi_{\text{base}}(\theta_{\text{base}}, \hat{y}_{k-n_a}^{k-1}, u_{k-n_b}^{k-1}) - \hat{x}_{b,k} \right\|_2^2, \quad (30)$$

where $\hat{x}_{b,k}$ is the forward simulated state of the baseline model in the extended dataset $\hat{\mathcal{D}}_N$. If augmented states are considered, the baseline encoder ψ_{base} is extended with an augmented state encoder ψ_{aug}

$$\begin{bmatrix} x_{b,k|k} \\ x_{a,k|k} \end{bmatrix} = \begin{bmatrix} \psi_b(\theta_{\text{base}}, \hat{y}_{k-n_a}^{k-1}, u_{k-n_b}^{k-1}) \\ \psi_a(\theta_{\text{aug}}, \hat{y}_{k-n_a}^{k-1}, u_{k-n_b}^{k-1}) \end{bmatrix}, \quad (31)$$

where the weights and biases of ψ_{aug} are initialised by the Xavier approach. The loss function (30) is no longer considered after initialisation.

5.4.3 LFR matrix and learning component initialisation

We now initialise the LFR matrix and the learning components so that (29) holds for initialisation. We can simplify this equation with Condition (b) by only considering the linear component of the learning function and initialising the NL component to be zero, i.e., $\phi_{\text{aug}}(z_{a,k}) = 0 + W_a z_{a,k}$. We

further assume under the acyclic property, without loss of generality, that D_{zw} is lower block diagonal with respect to the learning functions and the baseline model. This means that $D_{zw}^{aa} = 0$, $D_{zw}^{bb} = 0$, and either $D_{zw}^{ba} = 0$ or $D_{zw}^{ab} = 0$. Substituting the linear component of the learning function into (16) and eliminating $z_{a,k}$, gives

$$z_{b,k} = \underbrace{\left[C_z^b + D_{zw}^{ba} W_a C_z^a \quad D_{zu}^b + D_{zw}^{ba} W_a D_{zu}^a \right]}_{\tilde{C}} \begin{bmatrix} \hat{x}_k \\ u_k \end{bmatrix}, \quad (32)$$

and the prediction equation

$$\begin{bmatrix} \hat{x}_{k+1} \\ \hat{y}_k \end{bmatrix} = \underbrace{\begin{bmatrix} A + B_w^a W_a C_z^a & B_u + B_w^a W_a D_{zu}^a \\ C_y + D_{yw}^a W_a C_z^a & D_{yu} + D_{yw}^a W_a D_{zu}^a \end{bmatrix}}_A \begin{bmatrix} \hat{x}_k \\ u_k \end{bmatrix} + \underbrace{\begin{bmatrix} B_w^b + B_w^a W_a D_{zw}^{ab} \\ D_{yw}^b + D_{yw}^a W_a D_{zw}^{ab} \end{bmatrix}}_{\tilde{B}} \phi_{\text{base}}(z_{b,k}). \quad (33)$$

Thus, to have an initialisation satisfying (29), we require $\tilde{B} = I_{n_x+n_y}$ and $\tilde{C} = I_{n_x+n_u}$. We repeat here that we assume either $D_{zw}^{ba} = 0$ or $D_{zw}^{ab} = 0$ to satisfy Condition 6. The choice between these assumptions results in initialisation similar to the model structures derived in Appendix A, with $D_{zw}^{ba} = 0$ resulting in series output augmentations, $D_{zw}^{ab} = 0$ in series-input and $D_{zw}^{ba} = D_{zw}^{ab} = 0$ in parallel augmentation.

All matrices not required to set the baseline model behaviour at initialisation (29) have all elements m of the matrix initialised randomly, according to [32], i.e., $m \sim \mathcal{U}(-1, 1)$ where $\mathcal{U}(a, b)$ denotes a uniform distribution with support from a to b .

5.5 Convergence and Consistency

Next, we can analyse the statistical properties of the introduced augmentation approach in terms of convergence and consistency [24]. *Convergence* implies that, as the number of samples in \mathcal{D}_N tends to infinity, the empirical identification criterion approaches its expected value. An estimator is *consistent* if, as $N \rightarrow \infty$, the estimated model converges to an equivalent representation of the true system (1).

Under Conditions 2.1–2.4 in [5] on the data-generating process (1), model structure (6), and identification criterion (22), the convergence and consistency are proven. Condition 2.1 requires the data-generating system to be incrementally exponentially output stable, which becomes an assumption on the considered system (1). Similarly, Conditions 2.3 on predictor convergence and 2.4 on persistence of excitation are commonly assumed to hold. However, Condition 2.2 warrants additional consideration, as it demands differentiability of the model structure, including the encoder in (22), with respect to θ . This is not trivial due to the feedback connection in the model structure. If we take the acyclic condition (Condition (a)), then differentiability of $v(z_{b,k}, z_{a,k})$ is ensured, and it remains only to assume differentiability of the prediction mappings (6a), ϕ_{base} , and ϕ_{aug} —a standard and

Table 3
Physical parameters of the 3-DOF MSD systems.

Body	Mass m_i	Spring k_i	Damper c_i	Hardening a_i
1	0.5 kg	100 $\frac{\text{N}}{\text{m}}$	0.5 $\frac{\text{Ns}}{\text{m}}$	100 $\frac{\text{N}}{\text{m}^3}$
2	0.4 kg	100 $\frac{\text{N}}{\text{m}}$	0.5 $\frac{\text{Ns}}{\text{m}}$	-
3	0.1 kg	100 $\frac{\text{N}}{\text{m}}$	0.5 $\frac{\text{Ns}}{\text{m}}$	-

Table 4
Approximate physical parameters 2-DOF MSD baseline model.

Body	Mass m_i	Spring k_i	Damper c_i
1	0.5 kg	95 $\frac{\text{N}}{\text{m}}$	0.45 $\frac{\text{Ns}}{\text{m}}$
2	0.4 kg	95 $\frac{\text{N}}{\text{m}}$	0.45 $\frac{\text{Ns}}{\text{m}}$

non-restrictive assumption in system identification. Thus, all conditions in [5] are fulfilled to imply convergence and consistency of the proposed model augmentation approach.

6 Simulation Study

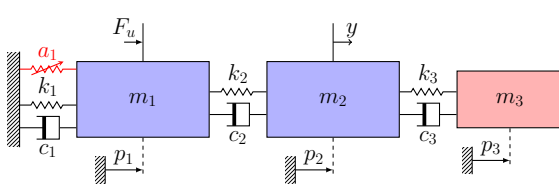
In this section, we analyse the performance of different model augmentation realisations of the LFR model when applied to various systems using a common baseline model. The objective is to demonstrate that the proposed LFR augmentation structure together with the proposed identification methods can effectively estimate system behaviour starting from the baseline model, while achieving faster estimation and offering greater transparency compared to the fully ANN-SS model. We focus here on structured parameterisations of the LFR in the form of those presented in Table 1 and Table 2. In Section 7, this analysis is extended to flexible parameterisations, applied to a real-world setup with a more complex baseline model, where the most suitable form of augmentation is not known a priori.

6.1 Mass-Spring-Damper system and data generation

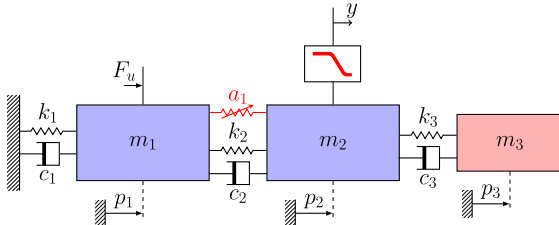
As a simulation example, a *mass–spring–damper* (MSD) system consisting of three masses is considered under three different configurations, as illustrated in Fig. 7. The corresponding physical parameters are listed in Table 3. Configuration (a) consists of three masses and a hardening spring nonlinearity. Configurations (b) and (c) add to this an input saturation and a first-order low-pass filter (LPF) to the output, respectively.

Configuration (a) is described in terms of a state-space representation with a total of 6 states as the positions p_i and velocities \dot{p}_i of the masses m_1 , m_2 , and m_3 . The hardening spring nonlinearity is simulated as a cubic stiffness term multiplied by the parameter a_1 . The measured output corresponds to the position p_2 , and the external input force is applied to the first mass m_1 . For Configuration (b) the saturation is $30 \tanh(\frac{u}{30})$ which results in a reduction of the applied multisine input signal RMS from 10.0 N to 9.11 N. For Configuration (c), the LPF is simulated such that the Bode plot of the LPF component is as shown in Fig. 10.

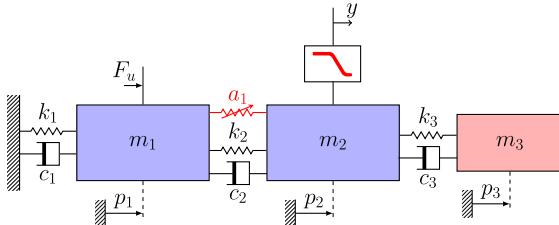
The system is simulated using a 4th order *Runge-Kutta* (RK4) numerical integration with step size $T_s = 0.02$ s and



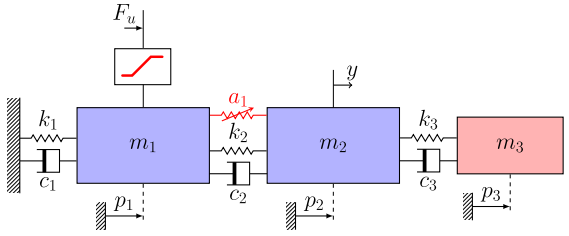
(a) 3-DOF MSD with nonlinear cubic spring



(b) 3-DOF MSD with nonlinear cubic spring and input saturation



(c) 3-DOF MSD with nonlinear cubic spring and low-pass filter



(d) 2-DOF MSD linear baseline model

Fig. 7. Considered baseline model in blue and black and the MSD data generating systems with additional dynamics in red.

Table 5

Hyperparameters for identifying the LFR-based augmentation and ANN-SS models.

hidden layers	nodes	n_a n_b	T	epochs	batch size
2	8	7	200	3000	2000

synchronised zero-order-hold actuation and sampling. The values of the DT input signal u_k are generated by a random-phase multisine with 1666 frequency components in the range $[0, 25]$ Hz with a uniformly distributed phase in $[0, 2\pi]$. The sampled output measurements y_k are perturbed by an additive white noise process $e_k \sim \mathcal{N}(0, \sigma_e^2)$. Here, σ_e is chosen so that the signal-to-noise ratio is equal to 30 dB. The generated sampled output y_k for the input u_k is collected in the data set \mathcal{D}_N . Separate data sets are created for estimation, validation and testing of different realisations of sizes $N_{\text{est}} = 2 \cdot 10^4$, $N_{\text{val}} = 10^4$, $N_{\text{test}} = 10^4$, respectively. The estimation data comprise two periods, while the validation and testing data each contain a single period.

6.2 Baseline model

The baseline model is chosen to represent the linear 2-DOF MSD dynamics shown in Fig. 7d. We consider two initialisations for the baseline model parameters: the ideal values from Table 3 and the approximate values from Table 4. The *root mean squared error* (RMSE) of the simulation responses of the baseline model for these initial parameter values is shown in Table 6 for configurations (a-c). Both initialisations perform relatively poorly, despite (approximately) representing a large part of the dynamics.

6.3 Config. (a): MSD with added cubic spring and mass

First, we consider the augmentation of the baseline model in a structured form using the introduced LFR model structure. For this we consider various parameterisations of the LFR matrix W corresponding to the configurations in Table 1 (not including S-SSI or S-DSI as we know a-priori that these will not model the system given the baseline model).

For parallel augmentation structures, the learning components are chosen as feedforward neural networks, and for series augmentation structures, we choose ResNets to have a feasible initialisation (see Section 5.4). For all learning components, the number of hidden layers and neurons are listed in Table 5. The activation function is chosen as tanh. For the dynamic augmentation, we add two additional states to the baseline model states for a total of 6 states. This is the minimum number of states required to completely model the 3-DOF MSD system. The baseline model, learning component, and encoder parameters are jointly estimated as described in Section 3. The hyperparameters for these estimations are shown in Table 5, with 16 nodes and 2 hidden layers used for the encoder. The regularisation tuning parameter λ in the joint identification cost function was set at $\lambda = 1$ for ideal initialisation. The identification criterion is optimised using Adam. As a comparison to a black-box approach, an ANN-SS model parameterised by ResNets is estimated with the SUBNET method [4] and hyperparameters from Table 5.

The simulation RMSE on the test data for these estimated models is shown in Table 6. The dynamic augmentations are able to capture the dynamics accurately, while the static augmentations result in slightly less accurate models.

In Fig. 8 we show the validation loss curves of select estimated models. The convergence speed of the ANN-SS and S-DSO models is slower than the S-DP model, while all models achieve similar RMSE scores.

The estimated physical parameters remain very close to the initialisation values for both the ideal and the approximate case. This is not desired behaviour for the approximate initialisations, indicating that the learning components are learning parts of the system dynamics that could be represented by the baseline model.

In Fig. 9, we show the comparison between the states \hat{x} of the S-DP model (—) and the outputs of the learning components

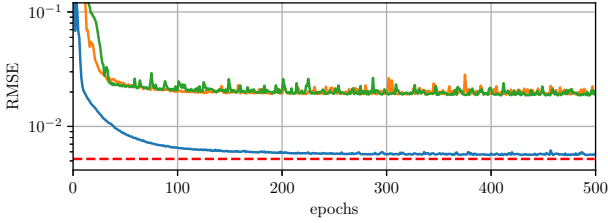


Fig. 8. Validation loss over first 500 training epochs for S-DP (—), S-DSO (—) and black-box ANN-SS (—) models estimated for the MSD system with configuration (a). The noise floor is shown with a red dashed line (---).

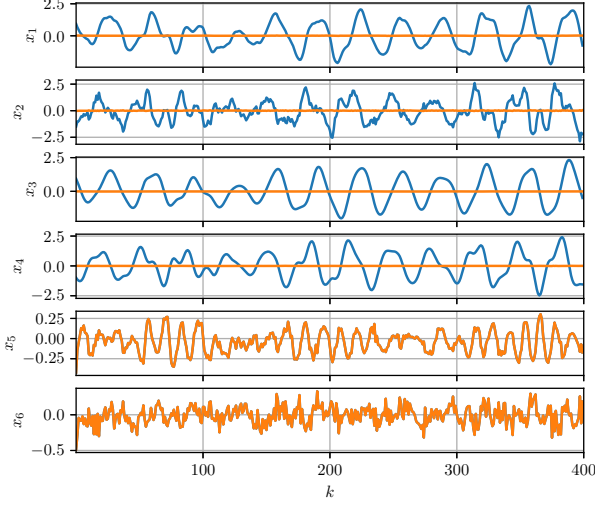


Fig. 9. Comparison of the augmented model with dynamic parallel configuration states \hat{x} (—) and the outputs of the learning components ϕ_{aug} (—) for a simulation with test data of the MSD system with configuration (a). States x_1 - x_4 are states of the augmented model based on the sum of f_{base} and f_{aug} , while states x_5 - x_6 are the output of the dynamic augmentation component g_{aug} .

ϕ_{aug} (—). Here, $x_b = [x_1^\top \dots x_4^\top]^\top$ and $x_a = [x_5^\top x_6^\top]^\top$. The effect of the learning components is relatively small for x_b , while x_a is modelled solely by the learning components. From this, we can conclude that the learning components are augmenting the baseline and not replacing the baseline model with their own dynamics.

6.4 Config. (b): MSD with added input saturation

For the MSD system in configuration (b), we applied similar identification steps as in Section 6.3. We again estimate S-SP and S-DP as described in Table 1. We, however, further combine these parameterisations with a series input augmentation to characterise the input saturation, which we note as S-SP-I with the following structure

$$x_{b,k+1} = f_{\text{base}}(x_{b,k}, g_{\text{aug}}(u_k)) + f_{\text{aug}}(x_{b,k}, u_k). \quad (34)$$

A similar structure is used for a S-DP with series input augmentation noted as S-DP-I. The remaining parameterisations and hyperparameters are as in Section 6.3. We again estimate an ANN-SS model parameterised by ResNets as a black-box comparison.

The simulation RMSE on the test data for these estimated models are shown in Table 6. All selected augmentations re-

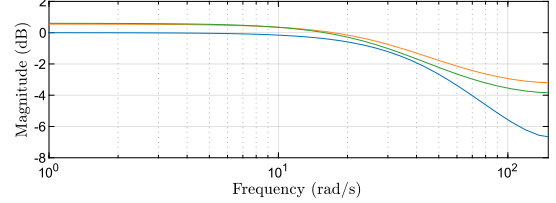


Fig. 10. Bode plot of both O-DSO estimated with the S-DP (—) and S-SP (—), compared against the LPF included in system configuration (c) (—).

sult in accurate models. However, the series input augmentation specifically models the input saturation as a function of u_k and thus results in a more interpretable model. The convergence of the estimated models are similar as in Fig. 8, with the S-SP-I and S-DP-I models converging faster than the backbox ANN-SS, S-SP and S-DP models.

6.5 Config. (c): MSD with added output low-pass-filter

For the MSD system in configuration (c), we applied similar identification steps as in Section 6.3. We again estimate the S-SP and S-DP described in Table 1. We now further estimate these state augmentations with an O-DSO described in Table 2. The O-DSO is parameterised by an LTI model with a single state, which is capable of modelling the dynamics of the first-order LPF. The remaining parameterisations and hyperparameters as in Section 6.3. We again estimate an ANN-SS model parameterised by ResNets as a black-box comparison.

The simulation RMSE on the test data for these estimated models is shown in Table 6. All selected augmentations result in accurate models. The convergence of the estimated models are similar as in Fig. 8, with the O-DSO models, S-DP and S-SP converging faster than the backbox ANN-SS model.

In Fig. 10, the Bode plot of h_{aug} from both the estimated O-DSO model, with S-SP and S-DP state models, are shown compared against the true system LPF. We can see that the output augmentations model behaviour similar to the system LPF thus enhancing the interpretability of the estimated model compared to the model augmentations without the output augmentation where this behaviour will have to be modelled in the state augmentation. Ensuring that output augmentations model the LPF exactly is an identifiability problem left to future research.

7 Experimental study

In this section, we demonstrate the capabilities of the general LFR-based model augmentation structure and the proposed estimation approach by identifying the dynamics of an F1Tenth electric vehicle, using experimental data.

7.1 F1Tenth vehicle

F1tenth is a 1/10 scale model of an electric car, which has been mainly developed as a test platform for various automotive applications [1]. To demonstrate the capabilities of the proposed LFR-based model augmentation structure, the dynamics of such a vehicle are identified in this section. In contrast to Section 6, measurements from a real F1tenth are

Table 6

RMSE of the simulated responses from the estimated models evaluated on the test sets generated by the MSD system with configurations (a), (b), and (c).

Model	Config. (a)		Config. (b)		Config. (c)	
	Ideal	Approx.	Ideal	Approx.	Ideal	Approx.
baseline	$1.97 \cdot 10^{-1}$	$1.77 \cdot 10^{-1}$	$1.96 \cdot 10^{-1}$	$1.86 \cdot 10^{-1}$	$2.22 \cdot 10^{-1}$	$2.13 \cdot 10^{-1}$
S-SP	$6.73 \cdot 10^{-3}$	$6.61 \cdot 10^{-3}$	$5.53 \cdot 10^{-3}$	$6.03 \cdot 10^{-3}$	$5.86 \cdot 10^{-3}$	$5.53 \cdot 10^{-3}$
S-DP	$5.54 \cdot 10^{-3}$	$5.77 \cdot 10^{-3}$	$5.79 \cdot 10^{-3}$	$5.80 \cdot 10^{-3}$	$5.46 \cdot 10^{-3}$	$5.39 \cdot 10^{-3}$
S-SSO	$7.07 \cdot 10^{-3}$	$6.80 \cdot 10^{-3}$	—	—	—	—
S-DSO	$5.33 \cdot 10^{-3}$	$5.57 \cdot 10^{-3}$	—	—	—	—
S-SP-I	—	—	$5.40 \cdot 10^{-3}$	$5.78 \cdot 10^{-3}$	—	—
S-DP-I	—	—	$5.44 \cdot 10^{-3}$	$5.41 \cdot 10^{-3}$	—	—
S-SP & O-DSO	—	—	—	—	$5.45 \cdot 10^{-3}$	$5.42 \cdot 10^{-3}$
S-DP & O-DSO	—	—	—	—	$5.39 \cdot 10^{-3}$	$5.38 \cdot 10^{-3}$
blackbox ANN-SS	$5.72 \cdot 10^{-3}$		$6.37 \cdot 10^{-3}$		$5.55 \cdot 10^{-3}$	

used instead of simulation data. An in-depth description of the used vehicle and test environment is available in [14].

7.2 Baseline model of the F1Tenth vehicle

To develop a baseline model of the F1Tenth platform, the so-called single-track model has been used [27]. The model is illustrated in Fig. 11, and can be expressed by using six state variables. The baseline states are the position of the *center-of-gravity* (CoG) in the (X, Y) plane (p_x, p_y), the orientation of the vehicle φ , which is measured from the X axis, the longitudinal and lateral velocities of the vehicle, and the yaw rate. The control inputs are the steering angle δ , and the PWM percentage of the electric motor that provides the main propulsion of the vehicle. The equations of the single-track model can be derived in continuous time, and the resulting model is discretised using the RK4 scheme. Since the used OptiTrack motion capture system measures the position and orientation of the vehicle, while the built-in IMU and speed sensors provide information regarding the velocity components, full state measurements are available. Hence, the baseline output function becomes $\hat{y}_k = x_{b,k}$. To model the longitudinal tire force component F_ξ , an empirical drivetrain model [14] is applied, while the linearised Magic Formula [26] has been utilised to model the lateral tire force components ($F_{f,\eta}$ and $F_{r,\eta}$). For a detailed derivation and discussion of the baseline model, refer to [13, 18].

The applied tire models (especially the empirical drivetrain model) are highly approximative and are the primary sources of inaccuracy in the baseline model; hence, identifying the dynamics of the F1Tenth vehicle is challenging even when incorporating existing physical knowledge into the model structure. Moreover, there are 9 baseline parameters (such as mass, inertia, distance of the rear and front end from the CoG, and parameters corresponding to the tire models) that need to be estimated. Initial values of these parameters were determined in [13]. However, some elements of this initial parameter vector θ_{base}^0 are highly approximative. Hence, to achieve an accurate representation of the true dynamics, θ_{base} is tuned jointly with the model parameters.

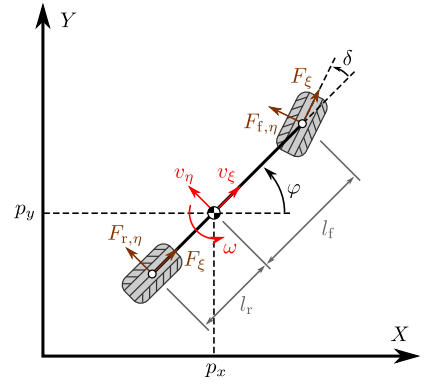


Fig. 11. Illustration of the single track model.

7.3 Data acquisition

A lemniscate-shaped trajectory has been selected for generating measurement data because, by following it, the heading angle traverses the whole operational domain, and the resulting motion has quick changes in velocity. A second trajectory has been chosen to be a circle-shaped path because it is also a typical maneuver for this type of vehicle. Measurement data has been collected with a sampling frequency of $f_s = 40$ Hz. To acquire data with various motor PWM inputs, the velocity references have been varied for both trajectories, ranging from 0.45 m/s to 1 m/s with step increments of 0.05 m/s, resulting in a total of 24 measurement records. Half of these measurements have been separated into training and test sets. Both trajectories with alternating reference velocities have been included in all data sets. Before concatenating the measurement signals for the training data set, contiguous segments (corresponding to 20% of the length of each of the 12 training signals) were randomly selected to form the validation data set. A total of 6467 samples are used for estimation, 1669 for validation, and 8041 for testing.

7.4 Estimated models

As proposed by [18, 36], to simplify the neural network structure, we only identify the input-to-velocity relationship

Table 7

Hyperparameters of the LFR-based model augmentation structure for identifying the dynamics of the F1Tenth vehicle.

hidden layers	nodes	n_a n_b	T	epochs	batch size
2	128	12	40	3000	256

by detaching the integrators. Hence, the outputs (and consequently, the baseline states) become the longitudinal and lateral velocity components, as well as the yaw rate of the vehicle. Then, after identification, by putting back the integrator dynamics, the position and orientation values can also be obtained during model simulation.

As all baseline model states are measured, the initial values of x_b are known for all subsections when calculating the truncated prediction loss, i.e., the encoder network only estimates the augmented states in case a dynamic model augmentation structure is applied. For the latter scenario, a fully-connected feedforward ANN with 2 hidden layers and 64 nodes per layer has been selected for the encoder network with the tanh activation function. Based on previous black-box identification results on the same dataset (see [36]), an encoder lag of $n_a = n_b = 12$ has been applied. The augmented state dimension has been selected based on physical insight and a short trial-and-error period as $n_{x_a} = 2$. For the LFR-based structure, $n_{z_a} = 4$ has been applied, while $n_{w_a} = 3$ and $n_{w_b} = 5$ were selected for the static and dynamic model augmentations, respectively. A regularisation coefficient of $\lambda = 0.01$ has been applied, as a result of a line-search. All other hyperparameters are summarised in Table 7.

As discussed in Remark 10, there are a few possible strategies to ensure the well-posedness of the LFR-based structure (6). The most straightforward one is to restrict $D_{zw} \equiv 0$, while a more general approach is to select either D_{zw}^{ba} or D_{zw}^{ab} to be tuned freely, while the rest of D_{zw} is set to zero. To demonstrate these approaches, we have trained models with different options regarding the structure of the D_{zw} matrix. Furthermore, we demonstrate the enforcing of model structures in the LFR matrix W by constraining the C_z^b and D_{zu}^b matrices such that $z_{b,k} \equiv \text{vec}(x_{b,k}, u_k)$, we have also trained models with that setting. The results are summarised in Table 8, where the augmented models are compared with state-of-the-art black-box identification results and the baseline model with nominal parameters. As the integrator dynamics make it difficult to obtain accurate long-term predictions in practice, the presented error values only consider the velocity components of the output. This is in line with previous black-box results using the same data set, see [36]. Still, to demonstrate the accuracy of the simulated position and orientation values, Fig. 12 presents these signals obtained using the best-performing static and dynamic LFR-based models for an arbitrarily selected test trajectory. Notably, both models demonstrate remarkable accuracy compared to the real measured data, even over extended open-loop simulations lasting 16–18 seconds. It is important to note that the reported errors are also influenced by the employed numerical integration scheme. This effect is particularly visible in the case of the dynamic LFR model, where the simulated tra-

Table 8

Normalised root mean squared simulation error of the estimated models on the F1Tenth identification study.

Model	Test NRMS error
static LFR-based ($D_{zw} \equiv 0$)	10.71%
static LFR-based (D_{zw}^{ab} tuned)	9.27%
static LFR-based (D_{zw}^{ba} tuned)	10.44%
static LFR-based ($D_{zw} \equiv 0, z_b$ fixed)	9.42%
static LFR-based (D_{zw}^{ab} tuned, z_b fixed)	9.90%
dynamic LFR-based ($D_{zw} \equiv 0$)	8.79%
dynamic LFR-based (D_{zw}^{ab} tuned)	8.52%
dynamic LFR-based (D_{zw}^{ba} tuned)	8.99%
dyn. LFR-based ($D_{zw} \equiv 0, z_b$ fixed)	8.25%
dyn. LFR-based (D_{zw}^{ab} tuned, z_b fixed)	8.41%
Initial baseline model	49.12%
DT SUBNET (black-box, [36])	8.53%
CT SUBNET (black-box, [36])	8.99%

jectory initially closely follows the measured data, but the accuracy continuously deteriorates due to the accumulation of integration errors and unknown input disturbances.

Further analysing the results shown in Table 8, it is visible that the most general options (not fixing z_b , and tuning D_{zw}^{ab}) have resulted in the best model accuracy for the static structure. As the applied approximative baseline model only expresses the dominant high-order dynamics of the real system, all dynamic augmentation structures have outperformed the static models. Introducing the augmented states in the LFR-based structure increases the model DoF compared to static structures. This helps explain why the highest accuracy for the dynamic LFR augmentation is obtained when certain constraints are imposed on the LFR matrix. This example highlights the importance of selecting the optimal model complexity: richer parametrisations can improve expressiveness, but overly flexible models may suffer from reduced robustness. Introducing suitable restrictions can lead to improved performance by mitigating variance effects. It is also worth noting that multiple dynamic LFR-based augmented models have resulted in better model accuracies than the black-box methods.

All model augmentation structures have shown similar convergence properties as the DT SUBNET approach (a state-of-the-art black-box identification method); however, the dynamic LFR-based method performed the best in terms of convergence speed. Hence, the proposed model augmentation structure was able to generate more accurate results with better convergence properties than black-box methods.

8 Conclusion

In this paper a novel general LFR-based model augmentation has been proposed that provides unified representation

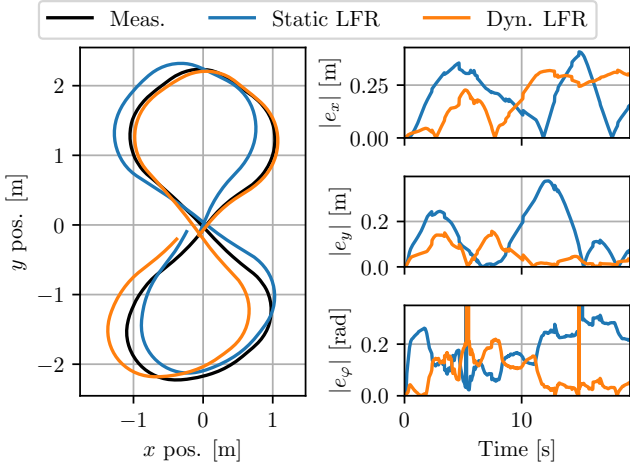


Fig. 12. Comparing the simulated model response with measurements on the test data.

structure. The model was also expressed in graph form, offering insight into the structural patterns that characterise and enable the detection of specific augmentation structures. In addition, we established conditions ensuring the well-posedness of the proposed model structure. To provide reliable estimation of the proposed model structure, an adaptation of the SUBNET approach was implemented, inheriting the consistency guarantees of the SUBNET approach. By analysing various augmentation configurations with simulation and experimental data, we have shown that suitable positioning of the learning component provides faster convergence and can lead to more accurate models compared to state-of-the-art black-box approaches.

Acknowledgements

We thank Mircea Lazar, Max Bolderman and Chris Verhoek for the helpful discussions for this work.

References

- [1] A. Agnihotri et al. Teaching Autonomous Systems at 1/10th-scale: Design of the F1/10 Racecar, Simulators and Curriculum. In *Proc. of the ACM Tech. Symp. on Comp. Sci. Edu.*, pages 657–663, 2020.
- [2] J. Bang-Jensen and G. Z. Gutin. *Digraphs: theory, algorithms and applications*. Springer, 2008.
- [3] F. L. Bauer. Computational graphs and rounding error. *SIAM Journal on Numerical Analysis*, 11(1):87–96, 1974.
- [4] G. I. Beintema. *Data-driven Learning of Nonlinear Dynamic Systems: A Deep Neural State-Space Approach*. Phd thesis, Eindhoven University of Technology, 2024.
- [5] G. I. Beintema, M. Schoukens, and R. Tóth. Deep subspace encoders for nonlinear system identification. *Automatica*, 156:111210, 2023.
- [6] C. M. Bishop. *Neural networks for pattern recognition*. Oxford university press, 1995.
- [7] T. P. Bohlin. *Practical grey-box process identification: theory and applications*. Springer, 2006.
- [8] M. Bolderman et al. Physics-guided neural networks for feedforward control with input-to-state-stability guarantees. *Control Engineering Practice*, 145:105851, 2024.
- [9] M. Bolderman, M. Lazar, and H. Butler. On feedforward control using physics-guided neural networks: Training cost regularization and optimized initialization. In *Proc. of the European Control Conf.*, pages 1403–1408, 2022.
- [10] M. Chioua (moderator). Machine learning and control. <https://www.youtube.com/watch?v=Jb7oU81QJPU> (42:15), 2021.
- [11] A. Daw et al. Physics-guided neural networks (pgnn): An application in lake temperature modeling. In *Knowledge Guided Machine Learning*, pages 353–372. Chapman and Hall/CRC, 2022.
- [12] L. El Ghaoui et al. Implicit deep learning. *SIAM Journal on Mathematics of Data Science*, 3(3):930–958, 2021.
- [13] K. Floch. *Model-based motion control of the FITENTH autonomous electrical vehicle*. Bachelor's thesis, Budapest University of Technology and Economics, 2022.
- [14] K. Floch et al. Gaussian-process-based adaptive tracking control with dynamic active learning for autonomous ground vehicles. *IEEE Transactions on Control Systems Technology*, pages 1–13, 2025.
- [15] D. Frank et al. Robust recurrent neural network to identify ship motion in open water with performance guarantees–technical report. *arXiv preprint arXiv:2212.05781*, 2022.
- [16] R.-S. Götte and J. Timmermann. Composed physics-and data-driven system identification for non-autonomous systems in control engineering. In *Proc. of the 3rd Int. Conf. on Artificial Intelligence, Robotics and Control*, pages 67–76, 2022.
- [17] W. D. Groote et al. Neural network augmented physics models for systems with partially unknown dynamics: Application to slider-crank mechanism. *IEEE/ASME Transactions on Mechatronics*, 27:103–114, 2 2022.
- [18] B. M. Györök et al. Orthogonal projection-based regularization for efficient model augmentation. In *Proc. of the 7th Annual Learning for Dynamics & Control Conf.*, pages 166–178, 2025.
- [19] K. He et al. Deep residual learning for image recognition. In *Proc. of the IEEE Conf. on computer vision and pattern recognition*, pages 770–778, 2016.
- [20] J. H. Hoekstra et al. Learning-based model augmentation with LFRs. *European Journal of Control*, 86(A):101304, 2025.
- [21] A. Isidori. *Nonlinear control systems: an introduction*. Springer, 1985.
- [22] S. Janny et al. Learning reduced nonlinear state-space models: an output-error based canonical approach. In *Proc. of the 61st IEEE Conf. on Decision and Control*, pages 150–155, 2022.
- [23] S. G. Krantz and H. R. Parks. *The implicit function theorem: history, theory, and applications*. Springer, 2002.
- [24] L. Ljung. Convergence analysis of parametric identification methods. *IEEE Transactions on Automatic Control*, 23, 1978.
- [25] L. Ljung. Perspectives on system identification. *Annual Reviews in Control*, 34(1):1–12, 2010.
- [26] H. B. Pacejka. Chapter 4 - Semi-Empirical Tire Models. In *Tire and Vehicle Dynamics (Third Edition)*, pages 149–209. Butterworth-Heinemann, Oxford, 2012.
- [27] B. Paden et al. A survey of motion planning and control techniques for self-driving urban vehicles. *IEEE Transactions on Intelligent Vehicles*, 1(1):33–55, 2016.
- [28] M. Raissi, P. Perdikaris, and G. E. Karniadakis. Physics-informed neural networks: A deep learning framework for solving forward and inverse problems involving nonlinear partial differential equations. *Journal of Computational Physics*, 378:686–707, 2019.
- [29] M. Revay and I. Manchester. Contracting implicit recurrent neural networks: Stable models with improved trainability. In *Proc. of the 2nd Conf. on Learning for Dynamics and Control*, pages 393–403, 2020.
- [30] J. Schoukens and L. Ljung. Nonlinear system identification: A user-oriented road map. *IEEE Control Systems*, 39:28–99, 12 2019.

- [31] M. Schoukens. Improved initialization of state-space artificial neural networks. In *Proc. of the 2021 European Control Conf.*, pages 1913–1918, 2021.
- [32] M. Schoukens and R. Tóth. On the initialization of nonlinear LFR model identification with the best linear approximation. *IFAC-PapersOnLine*, 53(2):310–315, 2020.
- [33] P. Shah et al. Deep neural network-based hybrid modeling and experimental validation for an industry-scale fermentation process: Identification of time-varying dependencies among parameters. *Chemical Engineering Journal*, 441:135643, 8 2022.
- [34] M. F. Shakib et al. Computationally efficient identification of continuous-time lur'e-type systems with stability guarantees. *Automatica*, 136:110012, 2022.
- [35] B. Sun et al. A comprehensive hybrid first principles/machine learning modeling framework for complex industrial processes. *Journal of Process Control*, 86:30–43, 2020.
- [36] M. Szécsyi et al. Deep learning of vehicle dynamics. *IFAC-PapersOnLine*, 58(15):283–288, 2024.
- [37] R. Tóth. *Modeling and identification of linear parameter-varying systems*, volume 403. Springer, 2010.
- [38] J. Veenman, C. W. Scherer, and H. Körögölu. Robust stability and performance analysis based on integral quadratic constraints. *European Journal of Control*, 31:1–32, 2016.
- [39] E. Winston and J. Z. Kolter. Monotone operator equilibrium networks. *Advances in neural information processing systems*, 33:10718–10728, 2020.
- [40] K. Zhou, J. Doyle, and K. Glover. *Robust and Optimal Control*. Feher/Prentice Hall Digital. Prentice Hall, 1996.

A Proof of Theorem 2

We provide the proof by parts:

Parallel augmentation at the state level: Choose $n_{z_a} = n_{x_b} + n_u + n_{x_a}$ and $n_{w_a} = n_{x_b} + n_{x_a}$. Take $z_{b,k} \equiv \text{vec}(x_{b,k}, u_k)$ and $z_{a,k} \equiv \text{vec}(x_{b,k}, x_{a,k}, u_k)$. For $z_{b,k}$, this is achieved by setting

$$C_z^b = \begin{bmatrix} I_{n_{x_b}} & 0_{n_{x_b} \times n_{x_a}} \\ 0_{n_u \times n_{x_b}} & 0_{n_{x_b} \times n_{x_a}} \end{bmatrix}, \quad D_{zu}^b = \begin{bmatrix} 0_{n_{x_b} \times n_u} \\ I_{n_u} \end{bmatrix}, \quad (\text{A.1})$$

while D_{zw}^{bb} , and D_{zw}^{ba} are set to zero, while for $z_{a,k}$, this is achieved by setting

$$C_z^a = \begin{bmatrix} I_{n_{x_b} + n_{x_a}} & 0_{n_u \times (n_{x_b} + n_{x_a})} \end{bmatrix}^\top, \quad D_{zu}^a = \begin{bmatrix} 0_{(n_{x_b} + n_{x_a}) \times n_u} & I_{n_u}^\top \end{bmatrix}^\top,$$

and setting D_{zw}^{ab} , and D_{zw}^{aa} as zeros. Next, we take $\hat{x}_{k+1} \equiv w_{b,k} + w_{a,k}$. This is achieved by setting $B_w^b = I_{n_{x_b}}$, and setting A^{bb} , A^{ba} , B_u^b , and B_w^{ba} as zeros. Then, we have

$$\begin{bmatrix} x_{b,k+1} \\ x_{a,k+1} \end{bmatrix} = \begin{bmatrix} f_{\text{base}}(x_{b,k}, u_k) \\ 0_{n_{x_a} \times n_{x_a}} \end{bmatrix} + \phi_{\text{aug}}(x_{b,k}, x_{a,k}, u_k), \quad (\text{A.2})$$

which is equivalent to the dynamic parallel state augmentation structure. Moreover, since the dynamic parallel structure is a generalisation of the static parallel, selecting $n_{x_a} = 0$ results in the static parallel state augmentation structure

$$x_{b,k+1} = f_{\text{base}}(x_{b,k}, u_k) + \phi_{\text{aug}}(x_{b,k}, u_k). \quad (\text{A.3})$$

Series output augmentation at the state level: Choose $n_{z_a} = 2n_{x_b} + n_{x_a} + n_u$, and $n_{w_a} = n_{x_b} + n_{x_a}$. Take $z_{b,k} \equiv \text{vec}(x_{b,k}, u_k)$,

and $z_{a,k} \equiv \text{vec}(x_{b,k}, x_{a,k}, u_k, f_{\text{base}}(x_{b,k}, u_k))$. The former can be achieved by setting C_z^b , D_{zu}^b as in (A.1), and D_{zw}^{bb} , D_{zw}^{ba} as zeros. The latter can be realised by restricting

$$C_z^a = \begin{bmatrix} I_{n_{x_b} + n_{x_a}}^\top & 0_{(n_u + n_{x_b}) \times (n_{x_b} + n_{x_a})}^\top \end{bmatrix}^\top, \quad (\text{A.4})$$

$$D_{zu}^a = \begin{bmatrix} 0_{(n_{x_b} + n_{x_a}) \times n_u}^\top & I_{n_u}^\top & 0_{n_{x_b} \times n_u}^\top \end{bmatrix}^\top, \quad (\text{A.5})$$

$$D_{zw}^{ab} = \begin{bmatrix} 0_{(n_{x_b} + n_{x_a} + n_u) \times n_{x_b}}^\top & I_{n_{x_b}}^\top \end{bmatrix}^\top, \quad (\text{A.6})$$

and selecting D_{zw}^{aa} as a zero matrix. Then, by selecting A , B_u , and B_w^b as zero matrices and setting B_w^a an identity matrix, the resulting state transition function is

$$\hat{x}_{k+1} = \phi_{\text{aug}}(x_{b,k}, x_{a,k}, u_k, f_{\text{base}}(x_{b,k}, u_k)). \quad (\text{A.7})$$

By universal approximation properties, there exist such weights and biases for $\phi_{\text{aug}} = \begin{bmatrix} (\phi_{\text{aug}}^b)^\top & (\phi_{\text{aug}}^a)^\top \end{bmatrix}^\top$ such that

$$\begin{bmatrix} x_{b,k+1} \\ x_{a,k+1} \end{bmatrix} = \begin{bmatrix} \phi_{\text{aug}}^b(x_{b,k}, x_{a,k}, u_k, f_{\text{base}}(x_{b,k}, u_k)) \\ \phi_{\text{aug}}^a(x_{b,k}, x_{a,k}, u_k) \end{bmatrix}, \quad (\text{A.8})$$

which is equivalent to the dynamic series output state augmentation. Moreover, as we have shown previously, dynamic augmentation is a generalisation of static augmentation; hence, the structure also represents the static series output augmentation form at the state level.

Static series input augmentation at the state level: Choose $n_{z_a} = n_{x_b}$ and $n_{x_a} = 0$. Take $z_{a,k} \equiv \text{vec}(x_{b,k}, u_k)$ by setting C_z^a , D_{zu}^a , D_{zw}^{ab} , D_{zw}^{bb} , A , B_u , B_w^b and D_{zw}^{aa} as for the parallel augmentation at the state level structure. Set $B_w^a \equiv 0$, $C_z^b \equiv 0$, $D_{zu}^b \equiv 0$ and D_{zw}^{ba} as an identity matrix. This achieves

$$z_{b,k} = \phi_{\text{aug}}(x_{b,k}, u_k), \quad (\text{A.9})$$

$$x_{b,k+1} = f_{\text{base}}(z_{b,k}), \quad (\text{A.10})$$

which is equivalent to the static series input augmentation form at the state transition level.

Dynamic series input augmentation on the state level: Choose $n_{z_b} = n_{x_b} + n_{x_a} + n_u$. Take $z_{a,k} \equiv \text{vec}(x_{b,k}, x_{a,k}, u_k)$ by setting C_z^a , D_{zu}^a , D_{zw}^{ab} , D_{zw}^{bb} , A , B_u and D_{zw}^{aa} as for the parallel augmentation at the state level structure. Set $C_z^b \equiv 0$, $D_{zu}^b \equiv 0$ and set D_{zw}^{ba} as an identity matrix. Consider the output of the learning component to be split into two parts $\phi_{\text{aug}} = \begin{bmatrix} (\phi_{\text{aug}}^b)^\top & (\phi_{\text{aug}}^a)^\top \end{bmatrix}^\top$. This achieves

$$\begin{bmatrix} x_{b,k+1} \\ x_{a,k+1} \end{bmatrix} = \begin{bmatrix} x_{b,k+1} = f_{\text{base}}(\phi_{\text{aug}}^b(x_{b,k}, x_{a,k}, u_k)) \\ \phi_{\text{aug}}^a(x_{b,k}, x_{a,k}, u_k) \end{bmatrix}, \quad (\text{A.11})$$

which is equivalent to the dynamic series input augmentation form at the state transition level.

Output augmentation structures: The output augmentation formulations are similar in structure to the state augmentation cases, but the connection of the baseline and learning components happens at the output level. Following the previous arguments, it is straightforward to derive that all structures in Table 2 can be represented by (6), similarly to the structures in Table 1, which concludes the proof.